

Modeling and Simulation of Laser Processing of Particulate-Functionalized Materials

T. I. Zohdi¹

Received: 22 October 2015 / Accepted: 29 October 2015
© CIMNE, Barcelona, Spain 2015

Abstract The objective of this paper is to focus on one of the “building blocks” of additive manufacturing technologies, namely selective laser-processing of particle-functionalized materials. Following a series of work in Zohdi (Int J Numer Methods Eng 53:1511–1532, 2002; Philos Trans R Soc Math Phys Eng Sci 361(1806): 1021–1043, 2003; Comput Methods Appl Mech Eng 193 (6–8):679–699, 2004; Comput Methods Appl Mech Eng 196:3927–3950, 2007; Int J Numer Methods Eng 76:1250–1279, 2008; Comput Methods Appl Mech Eng 199:79–101, 2010; Arch Comput Methods Eng 1–17. doi:[10.1007/s11831-013-9092-6](https://doi.org/10.1007/s11831-013-9092-6), 2013; Comput Mech Eng Sci 98(3): 261–277, 2014; Comput Mech 54:171–191, 2014; J Manuf Sci Eng ASME doi:[10.1115/1.4029327](https://doi.org/10.1115/1.4029327), 2015; CIRP J Manuf Sci Technol 10:77–83, 2015; Comput Mech 56:613–630, 2015; Introduction to computational micromechanics. Springer, Berlin, 2008; Introduction to the modeling and simulation of particulate flows. SIAM (Society for Industrial and Applied Mathematics), Philadelphia, 2007; Electromagnetic properties of multi-phase dielectrics: a primer on modeling, theory and computation. Springer, Berlin, 2012), a laser-penetration model, in conjunction with a Finite Difference Time Domain Method using an immersed microstructure method, is developed. Because optical, thermal and mechanical multifield coupling is present, a recursive, staggered, temporally-adaptive scheme is developed to resolve the internal microstructural fields. The time step

adaptation allows the numerical scheme to iteratively resolve the changing physical fields by refining the time-steps during phases of the process when the system is undergoing large changes on a relatively small time-scale and can also enlarge the time-steps when the processes are relatively slow. The spatial discretization grids are uniform and dense enough to capture fine-scale changes in the fields. The microstructure is embedded into the spatial discretization and the regular grid allows one to generate a matrix-free iterative formulation which is amenable to rapid computation, with minimal memory requirements, making it ideal for laptop computation. Numerical examples are provided to illustrate the modeling and simulation approach, which by design, is straightforward to computationally implement, in order to be easily utilized by researchers in the field. More advanced conduction models, based on thermal-relaxation, which are a key feature of fast-pulsing laser technologies, are also discussed.

1 Introduction

Several industrialized countries have stressed the importance of advanced manufacturing and related innovative research tools to their economies. This strategy has highlighted the role that advanced manufacturing technologies, such as additive manufacturing, can play for developers of next generation systems. Industries stand to make great gains by understanding and adopting the latest tools and processes in advanced manufacturing. The dramatic increase in computational power for mathematical modeling and simulation opens the possibility that scientific computing can play a significant role in the analysis of many emerging complex manufacturing processes. However, for this goal to be realized, a central objective is to

✉ T. I. Zohdi
zohdi@me.berkeley.edu

¹ Department of Mechanical Engineering, 6117 Etcheverry Hall, University of California, Berkeley, CA 94720-1740, USA

develop computational tools which can allow engineers and scientists to quickly design and analyze new additive manufacturing processes, resulting in superior products, produced at lower overall operational costs.

In many cases, these manufacturing processes may involve complex multi-step stages which combine disparate techniques such as (additive) deposition of complex material onto a surface followed by laser processing of the material in targeted regions, in order to create structures that are very difficult to construct using classical manufacturing methods. One type of approach in additive manufacturing is based on deposition of particulate mixtures of materials (essentially composites) onto substrates and allowing them to cure, in order to build layers of surface materials. Such materials are often referred to as particle-functionalized material, whereby the particles are added to a base binding material to add desired function. The attractiveness of such an approach for large-scale applications has been facilitated by the fact that huge quantities of inexpensive, high-quality, particles for additive powder-based manufacturing processes, are readily available, due to advanced materials processing techniques such as (a) sublimation from a raw solid to a gas, which condenses into particles that are recaptured (harvested), (b) atomization of liquid streams into droplets by breaking jets of metal, (c) reduction of metal oxides and (d) precise comminution/pulverizing of bulk material. In addition to the deposition of such material onto a substrate, there are a number of related post-processes which make up a successful overall additive manufacturing process. *One key component is laser processing*, which utilizes high-intensity beams to heat the material to desired temperatures either to subsequently bond, soften, sinter, melt or ablate (Fig. 1), in a very targeted manner. Laser-based heating is quite attractive because of the degree of precision that it allows. Because of the monochromatic and collimated nature of lasers, they are an attractive, highly-controllable, way to process materials¹. The range of power of a typical industrial laser is relatively wide, ranging from approximately 100–10,000 W. For example, carbon dioxide (CO_2) and yttrium aluminum garnet (YAG) lasers are commonly used. Typically, the initial beam produced is in the form of collimated (parallel) rays that are 1–2 mm apart, which are then focussed with a lens onto a small focal point (approximately 50 mm away) of no more than about 0.00001 m in diameter.

Remark 1 In 2014, related print-like additive manufacturing technologies, employing deposition of particulate materials, including ceramics, metals, plastics, organic, and

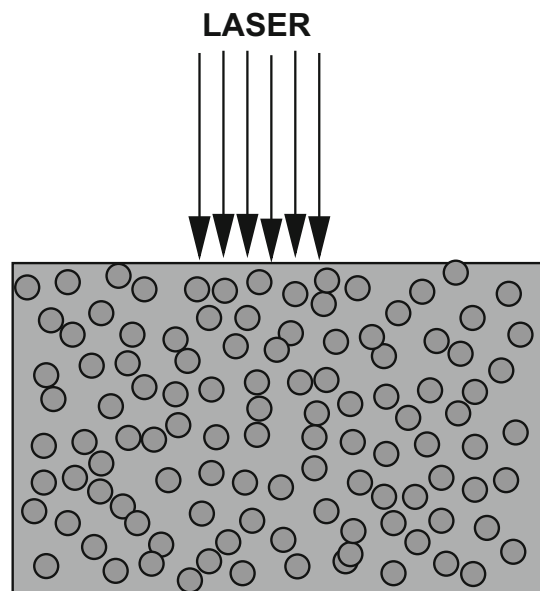


Fig. 1 A schematic of laser input applied to a particulate-functionalized material

even biological materials were a 2.2 billion dollar industry, with applications ranging from commercial manufacturing, medical technology, art and academia.² Applications include, for example, optical coatings and photonics (Nakanishi et al. [58]), MEMS applications (Fuller et al. [27], Samarasinghe et al. [72] and Gamota et al. [28]) and Biomedical devices (Ahmad et al. [4]). In terms of processing techniques, we refer the reader to Sirringhaus et al. [79], Wang et al. [85], Huang et al. [37], Choi et al. [14–17] and Demko et al. [19, 20] for details. These types of applications and associated technology are closely related to those in the area of spray coatings, and we refer the reader to the extensive works of Sevostianov and Kachanov [74–76], Nakamura and coworkers: Dwivedi et al. [25], Liu et al. [51, 52], Nakamura and Liu [59], Nakamura et al. [60] and Qian et al. [67] and to Martin [53, 54] for the state of the art in deposition technologies. We refer the reader to the recent overview article by Huang et al. [36] on the wide array of activities in the manufacturing community in this area.

Remark 2 There are a variety of other techniques that may be involved in an overall additive manufacturing processes, such as: (a) electron beam melting, which is a process where the deposited material is bonded together layer per layer with an electron beam in a high vacuum, (b) aerosol jetting, which directs streams of atomized

¹ In particular with pulsing, via continuous beam chopping or modulation of the voltage.

² A rough market percentage breakdown is 30 % motor vehicles, 15 % consumer products, business 11 %, medical 9 and 35 % spread across other fields. Three-dimensional printing was pioneered in 1984 by Hull [38] of the 3D-Systems Corporation.

particles at high velocities towards a substrate and (c) inkjet printing, which works by projecting small droplets of ink towards a substrate through a small orifice by pressure, heat, and vibration. The deposited material is then heated by UV light or other means to rapidly dry.

1.1 Objectives of this Paper

One concern of manufacturers is the microstructural defects generated in additively manufactured products, created by imprecisely controlled heat affected zones, brought on by miscalibration of the laser power needed for a specific goal. For example, due to the rise of one particular branch of additive manufacturing, printed flexible electronics, involving sensitive substrates, it has become important to precisely understand how much laser-input is needed. Furthermore, in many cases one may need to pulse the laser, either for technological reasons, such as to avoid overheating, or to activate certain thermal relaxation effects, which are discussed later. In particular, because many substrates can become thermally-damaged, for example from thermal stresses, ascertaining the appropriate amount of laser input is necessary. Thus, in order for *emerging additive approaches to succeed, one must draw upon rigorous theory and computation to guide and simultaneously develop design rules for upscaling to industrial manufacturing levels. This motivates the present analysis.* The objective of this paper is to focus on one of the “building blocks” of additive manufacturing technologies, namely the laser-processing of complex particulate-functionalized materials. *This paper focusses on one key component of an overall additive manufacturing process—namely the subprocess of targeted laser energy input.* During the course of the analysis, key parameter groups are identified in order to determine the relative contribution of each type of physics. A thermo-mechanical continuum formulation, utilizing a modified Beer-Lambert laser penetration model is then developed and solved with a Finite Difference Time Domain (FDTD) Method in conjunction with an immersed microstructure method. Numerical examples are provided to illustrate the model’s behavior, which, by design, is straightforward to computationally implement, in order to be easily utilized by researchers in the field.

Remark Importantly, we note that within the last decade, technological advances have enabled the reliable control of ultrafast pulsed lasers to activate small-time scale heat wave effects. These effects are often referred to as thermally-relaxed “second-sound” effects, because of their mathematical similarity to wave propagation in acoustics, although normal sound waves are fluctuations in the density of molecules in a substance while thermally-relaxed

second-sound waves are fluctuations in the density of phonons. Such phenomena are predicted by models which introduce thermal relaxation times into heat-conduction relations. The thermally-relaxed second-sound is a quantum mechanical phenomenon in which heat transfer occurs by wave-like motion, rather than by the more usual mechanism of diffusion. This leads to a very high confinement of thermal energy in very targeted zones. Thermally-relaxed phenomena can be observed in any system in which most phonon–phonon collisions conserve momentum, and can play a role when the time scale of heat input is quite small. More advanced models, based on thermal-relaxation, which are a key feature of fast-pulsing laser technologies, are discussed in the summary.

2 Initial Analysis: Qualitative Behavior-Response to Laser Input

In order to fully grasp the governing physical mechanisms in the upcoming analysis, we first analyze a simplified qualitative model, in order to determine their relative contribution.

2.1 A Simplified Analysis

The most basic type of conduction model is the classical Fourier-type:

$$\mathbf{q}_k = -\mathbb{K} \cdot \nabla \theta, \quad (2.1)$$

where θ is the temperature, \mathbf{q}_k is the conductive heat flux, \mathbb{K} is the thermal conductivity. A balance of power, momentarily ignoring the effects of deformation and stress reads as

$$\rho \dot{w} = \rho C \frac{\partial \theta}{\partial t} = -\nabla \cdot \mathbf{q}_k + \mathcal{S}, \quad (2.2)$$

where ρ is the mass density, $w = C(\theta - \theta_o)$ is the stored thermal energy, θ_o is a reference temperature, C is the heat capacity and \mathcal{S} represents other sources, *such as laser energy input.* In order to simplify the analysis, we consider an isolated small spherical particle. We employ a lumped mass model shown in Fig. 2 (a control volume inside the dashed lines). We remark that the validity of using a lumped thermal model for a particle, i.e. ignoring temperature gradients and assuming a uniform temperature within a particle, is dictated by the magnitude of the Biot number. A small Biot number (significantly less than unity) indicates that such an approximation is reasonable. The Biot number for spheres scales with the ratio of particle volume ($V = \frac{4}{3}\pi r^3$) to particle surface area ($A_S = 4\pi r^2$), $\frac{V}{A_S} = \frac{r}{3}$ (r is the particle radius), which indicates that a

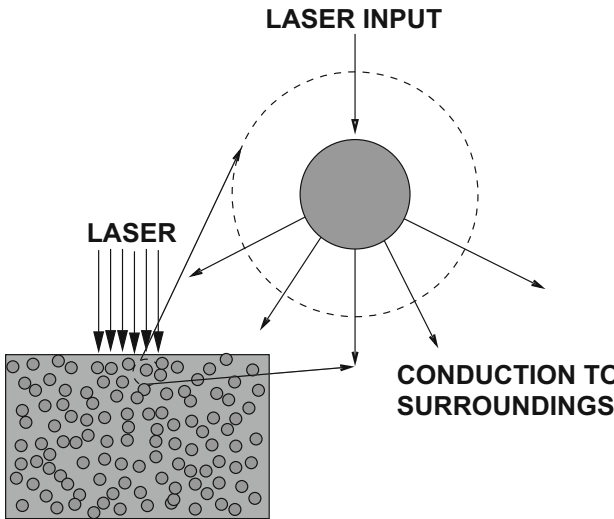


Fig. 2 A schematic of laser input applied to a particulate composite material

uniform temperature distribution is appropriate, since the particle is considered small. The governing equation, given by an overall energy balance (First Law of Thermodynamics) is

$$\dot{\theta} = \frac{\mathbb{K}A_S}{MCh}(\theta_S - \theta) + \frac{(1-R)I^i(t)A_L}{MC}, \quad (2.3)$$

where M is the mass of the particle and h is a length-scale for conduction (essentially the radius of the particle) and

- The absorbed incident optical radiation is $I^a(t)A_L = (I^i - I^r)A_L = (1-R)I^iA_L$, where I^a is the absorbed radiation per unit area, $I^r = RI^i$ is the reflected radiation, R is the reflectivity, $I^i = P/A_B$ is the incident radiation per unit area, P being the power (Watts), A_B is the area of the beam and A_L is the area of the exposed (laser irradiated) surface.
- The conduction to the surrounding is $\frac{\mathbb{K}}{h}(\theta_S - \theta)A_S$, where θ is the temperature of the material, θ_S is the temperature of the body to which the material is attached, A_S is the area of the surrounding surface that conducts heat, \mathbb{K} is the effective conductivity and h is the length scale over which the conduction occurs, which will be taken to be the radius of the particle.

2.2 Solution Character

For simple cases, this model can be solved analytically, for example for a constant laser input $I^i(t) = I^i$ (assuming $\theta(t=0) = \theta_S$)

$$\theta(t) = \theta_S + \frac{(1-R)I^iA_Lh}{\mathbb{K}A_S} \left(1 - e^{-\frac{\mathbb{K}A_S t}{MCh}}\right). \quad (2.4)$$

The relation above is important since it provides a qualitative relation that connects the temperature, to the laser input, conductivity, contact area and time. For example, if one set the desired temperature at a desired time to be $\theta(t^*) = \theta^*$ one can solve for the laser input needed

$$I^{*,i} = \frac{(\theta^* - \theta_S)\mathbb{K}A_S}{(1-R)A_Lh \left(1 - e^{-\frac{\mathbb{K}A_S t^*}{MCh}}\right)}. \quad (2.5)$$

We have the following observations:

- The rise time for the temperature is dictated by the ratio of conduction to heat capacity, $\frac{\mathbb{K}A_S}{MCh}$.
- At steady-state, $e^{-\frac{\mathbb{K}A_S t}{MCh}} \rightarrow 0$, and

$$\theta(t) = \theta_S + \frac{(1-R)I^iA_Lh}{\mathbb{K}A_S}, \quad (2.6)$$

which indicates that the ratio of $I^a = (1-R)I^i$ to $\frac{h}{\mathbb{K}}$ dictates the steady state temperature (assuming $A_L \approx A_S$).

- For a highly conductive surrounding: $\mathbb{K} \rightarrow \infty$, $\theta(t) = \theta_S$, where the conductive losses are instantaneous. This will draw heat away from the targeted zone.
- For a poorly conductive surrounding: $\mathbb{K} \rightarrow 0$, $\theta(t) = \theta_S + \frac{(1-R)I^iA_Lt}{MC}$, where the conductive losses are zero. This will trap (maximize) heat in the targeted zone.

2.3 Order of Magnitude Analysis

The ratios of the contributing terms are (leaving the dimensions of the target and the laser-power as variables):

$$\begin{aligned} \frac{\text{CONDUCTION}}{\text{LASER - IRRAD.}} &= \frac{\mathbb{K}(\theta_S - \theta)A_S}{h(1-R)I^iA_L} \approx \frac{\mathcal{O}(10^2)\mathcal{O}(10^2)A_S}{(1-R)I^iA_Lh} \\ &\approx \frac{\mathcal{O}(10^4)}{(1-R)I^ih}, \end{aligned} \quad (2.7)$$

where the ratio of the areas is assumed to be of order unity ($A_L \approx A_S$). Rewriting the irradiance per unit area in terms of power input, $(1-R)I^i = \frac{P}{A_L}$, yields

$$\frac{\text{CONDUCTION}}{\text{LASER - IRRAD.}} \approx \frac{\mathcal{O}(10^4)}{P \frac{h}{A_L}}, \quad (2.8)$$

and thus since $A_L \propto \pi h^2$ (h is effectively the radius of the particle)

$$\frac{\text{CONDUCTION}}{\text{LASER - IRRAD.}} \approx \frac{\mathcal{O}(10^4)h}{P}. \quad (2.9)$$

For example, for an idealized spherical particle, we have (Fig. 1)

- $A_S = \beta 4\pi r^2$, where $0 \leq \beta \leq 1$,
- $A_L = \pi r^2$.

For $r \approx h$, this yields $\frac{A_L}{h} \approx \mathcal{O}(r)$. Thus, for a small target, for example $r \approx 10^{-3}$ m, $P \approx 10^3$ W, then

$$\frac{\text{CONDUCTION}}{\text{LASER - IRRAD.}} \approx \mathcal{O}(10^{-2}). \quad (2.10)$$

Thus, the laser input is 100 times larger than conduction.

3 Formulations for Particulate-Laden Continua

The preceding analysis was of a generic isolated particle being irradiated by a laser and conducting heat with its surroundings based on a balance of energy in conjunction with Fourier-type conduction. To reliably extend this work, to particulate-based continua (multiple particles in a binding matrix), the spatial propagation of the thermal fields through conduction, and the resulting stress fields, require the use of spatial discretization techniques such as the Finite Difference Time Domain Method. The specific manufacturing scenario that we are interested in modeling is a particulate-functionalized composite material which experiences laser-pulsing in a targeted region. This covers a wide range of applications in additive manufacturing. Of particular interest is the resolution of thermal and residual stresses. Accordingly, this section is concerned with the computational characterization of the evolution of thermal and stress fields, in materials with particulate-functionalized microstructure. The objective of this work is to develop a straightforward computational framework that researchers in the field can easily implement and use as a computationally-efficient design tool. Generally speaking, there is a thermo-mechanical multifield coupling present, along with material changes associated with material hardening, elasto-plasticity and mechanical damage. Specifically, a recursively staggered, temporally-adaptive, FDTD (Finite Difference Time Domain) scheme is developed to resolve the internal microstructural thermal and mechanical fields, accounting for the simultaneous elasto-plasticity and damage. The time step adaptation is constructed to allow the numerical scheme to iteratively resolve the changing physical fields by reducing the time-steps during phases of the process when the system is undergoing changes on relatively small time-scales and also to enlarge the time-steps when the processes are relatively slow. The spatial discretization grids are uniform

and dense, with the complex microstructure being embedded into the mesh. The regular grid allows one to generate a matrix-free iterative formulation which is amenable to rapid computation and minimal memory requirements, making it ideal for laptop computation. The presentation is broken into four main parts: (1) characterization of the laser input, (2) formulations for each field in the model problem, identifying the coupling terms, (3) iterative staggering schemes (including spatial and temporal discretization) and (4) numerical examples for the model problem. The approach builds on work found in Zohdi [90–104] and then applies it to particle mixture deposition systems.

Remarks In this section, we focus on the thermo-mechanical response of a particulate mixture. The initial dynamic deposition process of multibody and inter-particle collisions is outside the scope of the present work. However, we mention in passing that to model the dynamics of particle systems, reduced-order particle-based or discrete element-based models, which treat such systems as multi-body dynamical groups, are often used. They are advantageous in dealing with domains that break apart or coalesce, as compared to traditional continuum based finite difference and finite element methods, which have limitations when dealing with dynamic discontinua. For reviews see, for example, Duran [24], Pöschel and Schwager [65], Onate et al. [62, 63], Rojek et al. [70], Carbonell et al. [13], Labra and Onate [46], Leonardi et al. [47], Cante et al. [12], Rojek [71], Onate et al. [64], Bolintineanu et al. [3], Campello and Zohdi [10, 11], Avci and Wriggers [2] and Zohdi [89–103]. In many cases, the deposition of these materials is the first stage of a multistep process which may involve, among other processes, compaction. Compaction is also somewhat outside the scope of the present work, and we refer the reader to Akisanya et al. [5], Anand and Gu [6], Brown and Abou-Chedid [9], Domas [21], Fleck [26], Gethin et al., [29], Gu et al. [32], Lewis et al. [48], Ransing et al. [68], Tatzel [80] and Zohdi [89–103]

3.1 Laser Input

Selective laser processing/sintering, was pioneered by Householder [35] in 1979 and Deckard [18] in the mid-1980's.³ Generally, an overall technological goal is to develop computational tools to accelerate the manufacturing of printed electronics. *Lasers can play a central role in precisely processing these systems.* To describe the *laser-target* interaction, the following must be accounted for: (a) absorption of laser energy input, (b) beam interference

³ A closely related method, Electron Beam Melting, fully melts the material and produces dense solids that are void free.

(attenuation) from the heterogeneous media and (c) heat transfer by conduction. There are varying degrees of sophistication for modeling the heat input from a laser, for example (Zohdi [89–103]). We utilize the Beer–Lambert law, whereby one performs an overall power balance (Fig. 6):

$$(I + \Delta I) - I + \mathcal{L}\Delta z = 0 \Rightarrow \frac{dI}{dz} = \mathcal{L} \approx -\alpha I, \quad (3.1)$$

where $\mathcal{L} \approx \alpha I$ is the absorbed irradiance (per unit area) from the laser and $z = z^*$ is the penetration location depth, which is solved to yield

$$I(z^*) = I_o e^{-\int_0^{z^*} \alpha dz}. \quad (3.2)$$

This is then incorporated into the First Law of Thermodynamics.

Remark We could perform a discretization of the irradiant beam into rays and perform a full-blown ray-tracking scheme (see Zohdi [89–103]), or perform a discretization of the beam into its electromagnetic field components via Maxwell's equations (see Zohdi [89–103]). While such approaches provide extremely detailed field information at the smallest scales, they are extraordinarily computationally expensive, and for the applications in this work, unwarranted. The Beer–Lambert framework provides an approach that is useful for practical computation. In such an approach, one can easily introduce nonuniform beam profiles, for example

$$I(r) = I(r=0)e^{-c||\mathbf{r}-\mathbf{r}_o||}, \quad (3.3)$$

where $||\mathbf{r}-\mathbf{r}_o||$ is the distance from the center of the incident beam line. In the case of $c = 0$ we recapture a flat beam, $I(r) = I(r=0)$.

3.2 Transient Thermo-Mechanical Coupled Fields

Following, Zohdi [89–103], we consider a model problem of a particulate composite (Fig. 1). The essential field equations and simplifying assumptions that will be used during the analysis are provided next.

3.2.1 Balance of Linear Momentum

We consider a balance of linear momentum governed by

$$\nabla_x \cdot \boldsymbol{\sigma} + \mathbf{f} = \rho \frac{d^2 \mathbf{u}}{dt^2}, \quad (3.4)$$

in regimes where *infinitesimal deformations are appropriate*, where $\boldsymbol{\sigma}$ is the Cauchy stress, \mathbf{f} are body forces, ρ is the material density and \mathbf{u} is the displacement. Consistent with the infinitesimal deformation approximation we write $\nabla_x \approx \nabla_X$ and $\frac{d(\cdot)}{dt} \approx \frac{\partial(\cdot)}{\partial t}|_X$, where X are the referential

coordinates, x are the current coordinates. We consider a damaged, elasto-plastic, isotropic constitutive law given by

$$\boldsymbol{\sigma} = \mathcal{D}\mathbb{E}_0 : (\boldsymbol{\epsilon} - \boldsymbol{\epsilon}_\theta - \boldsymbol{\epsilon}_p). \quad (3.5)$$

Under infinitesimal deformation framework, the balance of linear momentum becomes ($\rho \approx \rho_o$)

$$\nabla_X \cdot (\mathcal{D}\mathbb{E}_0 : (\boldsymbol{\epsilon} - \boldsymbol{\epsilon}_\theta - \boldsymbol{\epsilon}_p)) + \mathbf{f} = \rho_o \frac{\partial^2 \mathbf{u}}{\partial t^2} \quad (3.6)$$

with infinitesimal strains given by $\boldsymbol{\epsilon} = \frac{1}{2}(\nabla_X \mathbf{u} + (\nabla_X \mathbf{u})^T)$, thermal strains given by $\boldsymbol{\epsilon}_\theta \stackrel{\text{def}}{=} \gamma \cdot (\theta - \theta_0)\mathbf{1}$ and plastic strains given by $\boldsymbol{\epsilon}_p$, generated by the following unilateral conditions ($a \geq 0$)

$$||\boldsymbol{\sigma}'|| > \sigma_y \Rightarrow \dot{\zeta} = a \left(\frac{||\boldsymbol{\sigma}'||}{\sigma_y} - 1 \right) \quad (3.7)$$

and

$$||\boldsymbol{\sigma}'|| \leq \sigma_y \Rightarrow \dot{\zeta} = 0 \quad (3.8)$$

where $\dot{\boldsymbol{\epsilon}}_p = \dot{\zeta} \frac{\boldsymbol{\sigma}'}{||\boldsymbol{\sigma}'||}$ and $\boldsymbol{\sigma}' = \boldsymbol{\sigma} - \frac{tr\boldsymbol{\sigma}}{3}\mathbf{1}$ is the deviatoric stress. Here, the (isotropic) damaged elasticity tensor is $\mathbb{E} = \mathcal{D}\mathbb{E}_0$, where \mathbb{E}_0 represents the “virgin” isotropic undamaged material, $0 \leq \mathcal{D} \leq 1$ is the scalar continuity (isotropic damage) parameter (Kachanov [41]), $\mathcal{D}(t=0) = 1$ indicates the initial undamaged state and $\mathcal{D} \rightarrow 0$ indicates a completely damaged state. The damage arising from mechanical and thermal sources is modeled as being governed by evolution over-stress functions of the form ($b \geq 0$)

$$||\boldsymbol{\sigma}'|| > \sigma_d \Rightarrow \dot{\mathcal{D}} = b \left(\frac{||\boldsymbol{\sigma}'||}{\sigma_d} - 1 \right) \quad (3.9)$$

and

$$||\boldsymbol{\sigma}'|| \leq \sigma_d \Rightarrow \dot{\mathcal{D}} = 0, \quad (3.10)$$

We note that the rate constants a and b and the critical stresses σ_y and σ_d are potentially spatially-variable. Clearly, further evolution laws can be written for other material property changes, such as the thermal conductivity, although only changes in the mechanical property \mathbb{E} are considered during the formulations to follow.⁴ In the case of material isotropy

$$\boldsymbol{\sigma} = \mathcal{D}(\lambda_0 tr(\boldsymbol{\epsilon} - \boldsymbol{\epsilon}_\theta - \boldsymbol{\epsilon}_p)\mathbf{1} + 2\mu_0(\boldsymbol{\epsilon} - \boldsymbol{\epsilon}_\theta - \boldsymbol{\epsilon}_p)), \quad (3.11)$$

where λ_0 is the undamaged Lame parameter and μ_0 is the undamaged shear modulus.

⁴ For further details on these types of phenomenological (damage) formulations, the interested reader is referred to the seminal work of Kachanov [41].

3.2.2 Balance of Energy

The interconversions of various forms of energy (mechanical, thermal, etc) in a system are governed by the first law of thermodynamics,

$$\rho\dot{w} - \sigma : \nabla_x \dot{\mathbf{u}} + \nabla_x \cdot \mathbf{q} - \rho z = 0, \quad (3.12)$$

where w is the stored energy per unit mass, which is a function of the temperature (θ) and elastic strain, ($\epsilon^e = \epsilon - \epsilon_\theta - \epsilon_p$), \mathbf{q} is heat flux, and ρz is the rate of energy absorbed from sources (for laser input, $\rho z = aI$). We employ the following for the stored energy (assuming infinitesimal deformations)

$$\rho w = W \approx \frac{1}{2}(\epsilon - \epsilon_\theta - \epsilon_p) : \mathbb{E} : (\epsilon - \epsilon_\theta - \epsilon_p) + \rho C\theta, \quad (3.13)$$

which implies

$$\begin{aligned} \rho\dot{w} = \dot{W} &= (\dot{\epsilon} - \dot{\epsilon}_\theta - \dot{\epsilon}_p) : \mathbb{E} : (\epsilon - \epsilon_\theta - \epsilon_p) \\ &\quad + \frac{1}{2}(\epsilon - \epsilon_\theta - \epsilon_p) : \dot{\mathbb{E}} : (\epsilon - \epsilon_\theta - \epsilon_p) + \rho C\dot{\theta} + \rho\dot{C}\theta \end{aligned} \quad (3.14)$$

and thus the first law becomes

$$\begin{aligned} \rho C\dot{\theta} &= \sigma : (\dot{\epsilon}_\theta + \dot{\epsilon}_p) - \frac{1}{2}(\epsilon - \epsilon_\theta - \epsilon_p) : \dot{\mathbb{E}} : (\epsilon - \epsilon_\theta - \epsilon_p) \\ &\quad + \nabla_x \cdot (\mathcal{K} \cdot \nabla_x \theta) + \rho z - \rho\dot{C}\theta \end{aligned} \quad (3.15)$$

where Fourier's law, $\mathbf{q} = -\mathcal{K} \cdot \nabla_x \theta$, has been used.

3.3 Iterative Staggering Scheme

Following Zohdi [89–103], we now develop a staggering solution framework to solve the coupled systems of interest. The general methodology is as follows (at a given time increment): (1) each field equation is solved individually, “freezing” the other (coupled) fields in the system, allowing only the primary field to be active and (2) after the solution of each field equation, the primary field variable is updated, and the next field equation is treated in a similar manner. For an “implicit” type of staggering, the process can be repeated in an iterative manner, while for an “explicit” type, one moves to the next time step after one “pass” through the system. We will employ implicit staggering. Specifically, for the thermo-mechanical system under consideration, consider an abstract setting, whereby one solves for the mechanical field, assuming the thermal field is fixed (L is a time-step counter and K is a staggering-step counter),

$$\mathcal{A}_1(\underline{\mathbf{u}}^{L+1,K}, \underline{\theta}^{L+1,K-1}) = \mathcal{B}_1(\underline{\mathbf{u}}^{L+1,K-1}, \underline{\theta}^{L+1,K-1}) \quad (3.16)$$

then one solves for the thermal fields, assuming the mechanical field fixed,

$$\mathcal{A}_2(\underline{\mathbf{u}}^{L+1,K}, \underline{\theta}^{L+1,K}) = \mathcal{B}_2(\underline{\mathbf{u}}^{L+1,K}, \underline{\theta}^{L+1,K-1}) \quad (3.17)$$

where the only underlined variable is “active” at that stage of the process. Within the staggering (iterative) scheme, implicit time-stepping methods (with time step size adaptivity) will be used throughout the upcoming analysis (described shortly). The process is driven by minimizing nondimensional relative iterative coupling error (of both fields) within a time-step (difference between successive iterations). A tolerance check determines whether the iterations should continue, or if the time steps should be adaptively reduced to increase the rate of convergence. The time steps can be increased if convergence occurs too quickly, thus allowing larger time-steps and faster simulations for a given iterative error tolerance. The details of this process are discussed shortly. Generally speaking, if a recursive staggering process is not employed (an explicit coupling scheme), the staggering error can accumulate rapidly. However, simply employing extremely small time steps, smaller than needed to control the discretization error, in order to suppress a (nonrecursive) staggering process error, can be computationally inefficient. Therefore, the objective of the next subsection is to develop a strategy to adaptively adjust, in fact maximize, the choice of the time step size in order to control the staggering error, while simultaneously staying below a critical time step size needed to control the discretization error. An important related issue is to simultaneously minimize the computational effort involved. We now develop a staggering scheme by extending an approach found in the work of Zohdi [89–103].

Remark 1 The symbol $\|\cdot\|$ will signify the $L_2(\Omega)$ -norm throughout this work. The nondimensional error metric for the mechanical field is (where we assume that the denominator is nonzero)

$$\varpi_u^K \stackrel{\text{def}}{=} \frac{\|\mathbf{u}^{L+1,K} - \mathbf{u}^{L+1,K-1}\|}{\|\mathbf{u}^{L+1,K} - \mathbf{u}^L\|}, \quad (3.18)$$

and for the thermodynamic field

$$\varpi_\theta^K \stackrel{\text{def}}{=} \frac{\|\theta^{L+1,K} - \theta^{L+1,K-1}\|}{\|\theta^{L+1,K} - \theta^L\|}. \quad (3.19)$$

Thereafter, we select the maximum *nondimensionalized* error for adaptivity

$$\varpi^{*,K} \stackrel{\text{def}}{=} \max(\varpi_u^K, \varpi_\theta^K), \quad (3.20)$$

Remark 2 Staggering schemes are widely used in the computational mechanics literature, dating back, at least, to Zienkiewicz [87] and Zienkiewicz et al. [88]. For in depth overviews, see the works of Lewis and Schrefler (Lewis et al. [49] and Lewis and Schrefler [50])) and a series of works by Schrefler and collaborators: Schrefler [73], Turska and Schrefler [82], Bianco et al. [8] and Wang and Schrefler [83].

3.3.1 Spatial Discretization of the Fields

Numerically, the components of the gradient of functions such as \mathbf{u} and θ are approximated by central finite difference stencils of the basic form (Fig. 11):

$$\frac{\partial u_i}{\partial x_j}|_x \approx \frac{u_i(x_j + \Delta x_j) - u_i(x_j - \Delta x_j)}{2\Delta x_j} \quad (3.21)$$

for each of the (x_1, x_2, x_3) -directions, in order to form the terms needed in $\nabla_x \mathbf{u}$ and $\nabla_x \cdot \boldsymbol{\sigma}$. This is a second-order accurate stencil. For a generic second order scheme spatial derivative, such as

$$\frac{\partial \sigma}{\partial x}|_x \approx \frac{\sigma(x + \frac{\Delta x}{2}) - \sigma(x - \frac{\Delta x}{2})}{\Delta x}, \quad (3.22)$$

where generically, for example with an arbitrary material coefficient $a(x) = \lambda(x)$ or $a(x) = \mu(x)$ (Fig. 3):

$$\sigma(x + \frac{\Delta x}{2}) \approx a(x + \frac{\Delta x}{2}) \underbrace{\frac{u(x + \Delta x) - u(x)}{\Delta x}}_{\frac{\partial u}{\partial x}|_{x+\frac{\Delta x}{2}}} \quad (3.23)$$

and

$$\sigma(x - \frac{\Delta x}{2}) \approx a(x - \frac{\Delta x}{2}) \underbrace{\frac{u(x) - u(x - \Delta x)}{\Delta x}}_{\frac{\partial u}{\partial x}|_{x-\frac{\Delta x}{2}}} \quad (3.24)$$

where

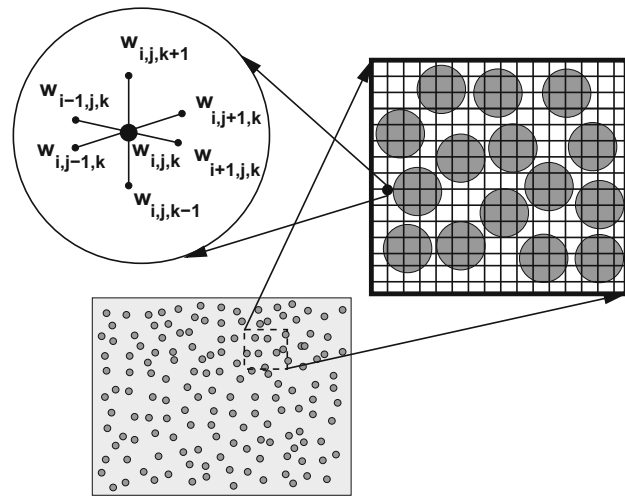


Fig. 3 A typical three dimensional finite-difference stencil for a field $w(x, y, z)$ (see Zohdi [89–103])

$$a(x + \frac{\Delta x}{2}) \approx \frac{1}{2}(a(x + \Delta x) + a(x)), \quad (3.25)$$

and

$$a(x - \frac{\Delta x}{2}) \approx \frac{1}{2}(a(x) + a(x - \Delta x)). \quad (3.26)$$

These approximations are made for all components and combinations in $\nabla_x \cdot \boldsymbol{\sigma}$. The mixed derivatives are derived in a similar manner in “Appendix 1”. Similarly, for a second order scheme spatial derivatives in the heat conduction

$$\frac{\partial q}{\partial x}|_x \approx \frac{q(x + \frac{\Delta x}{2}) - q(x - \frac{\Delta x}{2})}{\Delta x}, \quad (3.27)$$

where (in conjunction with Fourier’s Law)

$$q(x + \frac{\Delta x}{2}) \approx -\mathbb{K}(x + \frac{\Delta x}{2}) \underbrace{\frac{\theta(x + \Delta x) - \theta(x)}{\Delta x}}_{\frac{\partial \theta}{\partial x}|_{x+\frac{\Delta x}{2}}} \quad (3.28)$$

and

$$q(x - \frac{\Delta x}{2}) \approx -\mathbb{K}(x - \frac{\Delta x}{2}) \underbrace{\frac{\theta(x) - \theta(x - \Delta x)}{\Delta x}}_{\frac{\partial \theta}{\partial x}|_{x-\frac{\Delta x}{2}}} \quad (3.29)$$

where

$$\mathbb{K}(x + \frac{\Delta x}{2}) \approx \frac{1}{2}(\mathbb{K}(x + \Delta x) + \mathbb{K}(x)), \quad (3.30)$$

and

$$\mathbb{K}(x - \frac{\Delta x}{2}) \approx \frac{1}{2}(\mathbb{K}(x) + \mathbb{K}(x - \Delta x)). \quad (3.31)$$

These approximations are made for $\frac{\partial q_1}{\partial x_1}$, $\frac{\partial q_2}{\partial x_2}$ and $\frac{\partial q_3}{\partial x_3}$, in order to form the terms needed in $\nabla_x \cdot \mathbf{q}$. This is done at each node in the grid. See “Appendix 1” for more details.

3.4 Temporal Discretization of Fields

3.4.1 Mechanical Field

For the mechanical field (infinitesimal deformation formulation) we write

$$\frac{d\mathbf{v}}{dt} = \frac{\partial \mathbf{v}}{\partial t} = \frac{1}{\rho}(\nabla_x \cdot \boldsymbol{\sigma} + \mathbf{f}) \stackrel{\text{def}}{=} \boldsymbol{\Psi}. \quad (3.32)$$

We discretize for time $= t + \phi \Delta t$, and using a trapezoidal “ ϕ – scheme” ($0 \leq \phi \leq 1$, see “Appendix 3”)

$$\frac{\mathbf{v}(t + \Delta t) - \mathbf{v}(t)}{\Delta t} \approx \boldsymbol{\Psi}(t + \phi \Delta t) \approx \phi \boldsymbol{\Psi}(t + \Delta t) + (1 - \phi) \boldsymbol{\Psi}(t). \quad (3.33)$$

Rearranging, yields

$$\mathbf{v}(t + \Delta t) \approx \mathbf{v}(t) + \Delta t(\phi \Psi(t + \Delta t) + (1 - \phi)\Psi(t)) \quad (3.34)$$

where the previously introduced spatial discretization is applied to the terms in $\Psi (\nabla_x \cdot \boldsymbol{\sigma})$. Since this is a second-order system, the procedure is then repeated to determine the displacement field \mathbf{u} (see “Appendix 3”)

$$\begin{aligned} \mathbf{u}(t + \Delta t) &= \mathbf{u}(t) + \mathbf{v}(t + \phi\Delta t)\Delta t \\ &= \mathbf{u}(t) + (\phi\mathbf{v}(t + \Delta t) + (1 - \phi)\mathbf{v}(t))\Delta t, \end{aligned} \quad (3.35)$$

or more explicitly

$$\mathbf{u}(t + \Delta t) = \mathbf{u}(t) + \mathbf{v}(t)\Delta t + \phi(\Delta t)^2\Psi(t + \phi\Delta t). \quad (3.36)$$

The term $\Psi(t + \phi\Delta t)$ can be handled in two main ways:

- $\Psi(t + \phi\Delta t) \approx \Psi(\phi\mathbf{u}(t + \Delta t) + (1 - \phi)\mathbf{u}(t))$ or
- $\Psi(t + \phi\Delta t) \approx \phi\Psi(\mathbf{u}(t + \Delta t)) + (1 - \phi)\Psi(\mathbf{u}(t))$.

The differences are quite small between either of the above, thus, for brevity, we choose the latter. Therefore,

$$\begin{aligned} \mathbf{u}(t + \Delta t) &= \mathbf{u}(t) + \mathbf{v}(t)\Delta t \\ &\quad + \phi(\Delta t)^2(\phi\Psi(t + \Delta t) + (1 - \phi)\Psi(t)). \end{aligned} \quad (3.37)$$

When $\phi = 1$, then this approach can be considered to be a (implicit) Backward Euler scheme, which is very stable (very dissipative) and $\mathcal{O}((\Delta t)^2)$ locally in time, while if $\phi = 0$, the scheme can be considered as a (explicit) Forward Euler scheme, which is conditionally stable and $\mathcal{O}((\Delta t)^2)$ locally in time and if $\phi = 0.5$, then the scheme can be considered as a (implicit) Midpoint scheme, which is marginally stable and $\hat{\mathcal{O}}((\Delta t)^2) = \mathcal{O}((\Delta t)^3)$ locally in time. The dependent plastic and damage variables are also integrated in a similar manner

$$\boldsymbol{\epsilon}(t + \Delta t) = \boldsymbol{\epsilon}(t) + \Delta t(\phi\dot{\boldsymbol{\epsilon}}(t + \Delta t) + (1 - \phi)\dot{\boldsymbol{\epsilon}}(t)) \quad (3.38)$$

and

$$\mathcal{D}(t + \Delta t) = \mathcal{D}(t) + \Delta t(\phi\dot{\mathcal{D}}(t + \Delta t) + (1 - \phi)\dot{\mathcal{D}}(t)). \quad (3.39)$$

3.4.2 Thermal Fields

For the thermal field we write

$$\begin{aligned} \frac{\partial \theta}{\partial t} &= \frac{1}{\rho C} \left(\boldsymbol{\sigma} : (\boldsymbol{\epsilon}_\theta + \dot{\boldsymbol{\epsilon}}_p) - \frac{1}{2}(\boldsymbol{\epsilon} - \boldsymbol{\epsilon}_\theta - \boldsymbol{\epsilon}_p) : \right. \\ &\quad \left. \dot{\mathcal{E}} : (\boldsymbol{\epsilon} - \boldsymbol{\epsilon}_\theta - \boldsymbol{\epsilon}_p) + \nabla_X \cdot (\mathbb{K} \cdot \nabla_X \theta) + \rho z - \rho \dot{C} \theta \right) \stackrel{\text{def}}{=} \mathbf{Y}. \end{aligned} \quad (3.40)$$

We discretize for around the time $= t + \phi\Delta t$, yielding

$$\theta(t + \Delta t) \approx \theta(t) + \Delta t(\phi\mathbf{Y}(t + \Delta t) + (1 - \phi)\mathbf{Y}(t)), \quad (3.41)$$

where the previously introduced spatial discretization is applied to the terms in \mathbf{Y} .

3.5 The Overall Solution Scheme

In order to construct a solution, the algorithm is as follows:

- (1) *Spatio-temporal discretization* Construct derivative terms such as

$$\frac{\partial u(x)}{\partial x} \approx \frac{u(x + \Delta x) - u(x - \Delta x)}{2\Delta x}, \text{ etc} \quad (3.42)$$

and insert into the governing equations. This leads to a system of coupled equations, for each node $((i, j, k)$ in Fig. 4), which are cast in the following (implicit/recursive) form (which are a recasting of the abstract system (Eqs. 3.16–3.17))

$$\mathbf{u}(t + \Delta t) = \mathcal{F}(\mathbf{u}(t + \Delta t), \theta(t + \Delta t), \dots), \quad (3.43)$$

and

$$\theta(t + \Delta t) = \mathcal{Y}(\mathbf{u}(t + \Delta t), \theta(t + \Delta t), \dots). \quad (3.44)$$

- (2) *System staggering* Compute \mathbf{u} -field with θ -fields fixed, then compute θ -field with \mathbf{u} -fields fixed, etc, and iterate at time interval $L + 1, K = 1, 2, \dots$ for

$$\mathbf{u}^{L+1,K} = \mathcal{F}(\underline{\mathbf{u}^{L+1,K-1}}, \theta^{L+1,K-1}), \quad (3.45)$$

and

$$\theta^{L+1,K} = \mathcal{Y}(\underline{\mathbf{u}^{L+1,K}}, \underline{\theta^{L+1,K-1}}), \quad (3.46)$$

Solving each of the above Eqs. (3.45 and 3.46), with the respective other fields fixed, can be achieved in a variety of ways, for example iteratively or by direct (Gaussian-type) solution methods (Fig. 4). For example, an interior iterative loop, within the staggering loop (within a time-step), can be used to update the solution to solve the individual field, for example the mechanical field, before moving to the next field (for example the thermal field). Those internal iterations can be performed until that individual field converges. This can then be repeated for the next field. This would then complete one staggering iteration. There are of course many possible variants of this process. In theory, one could even simply perform an explicit update (no recursion). This is discussed further in the remarks that follow.

- (3) Compute error measures: $\varpi^{*,K} \stackrel{\text{def}}{=} \max(\varpi_u^K, \varpi_\theta^K)$, $i = 1, \dots, \text{nodes}$ in the system.
- (4a) If tolerance is met, $\varpi^{*,K} \leq C_{tol}$ and $K \leq K_d$, then:

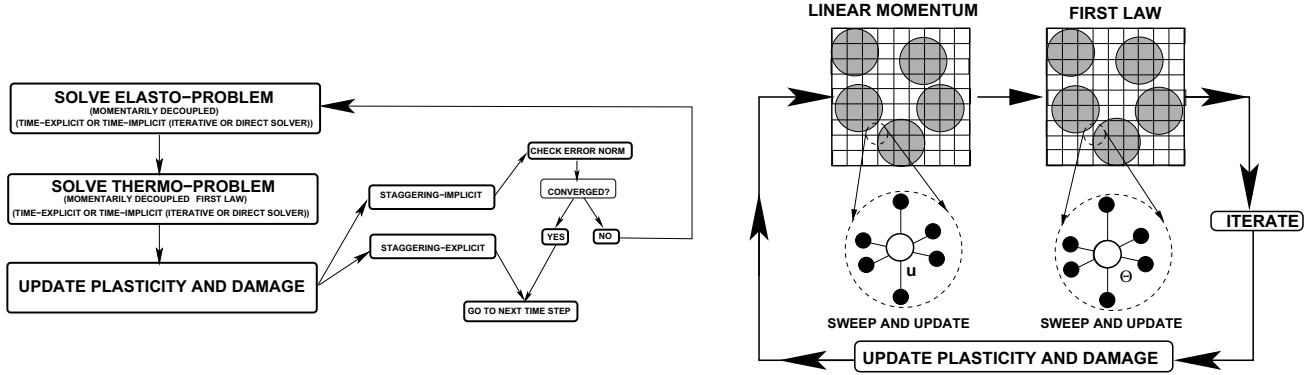


Fig. 4 The overall coupled staggering (*left*) solution and the matrix-free approach (*right*), following Zohdi [89–103]

- (1) Increment time forward: $t = t + \Delta t$,
- (2) Construct new time step: $(\Delta t)^{\text{new}} = \Phi_K(\Delta t)^{\text{old}}$,
where $\Phi_K \stackrel{\text{def}}{=} \begin{pmatrix} \left(\frac{C_{tol}}{\varpi^{*,0}}\right)^{\frac{1}{pK_d}} \\ \left(\frac{\varpi^{*,K}}{\varpi^{*,0}}\right)^{\frac{1}{pK}} \end{pmatrix}$
- (3) Select $\Delta t = \min((\Delta t)^{\text{lim}}, (\Delta t)^{\text{new}})$ and go to (1)
- (4b) If tolerance is not met, $\varpi^{*,K} > C_{tol}$ and $K = K_d$, then construct (refine) new time step: $(\Delta t)^{\text{new}} \stackrel{\text{def}}{=} \Phi_K(\Delta t)^{\text{old}}$, where $\Phi_K \stackrel{\text{def}}{=} \begin{pmatrix} \left(\frac{C_{tol}}{\varpi^{*,0}}\right)^{\frac{1}{pK_d}} \\ \left(\frac{\varpi^{*,K}}{\varpi^{*,0}}\right)^{\frac{1}{pK}} \end{pmatrix}$ and go to (1). This time-scaling relation is derived in “Appendix 2”.

At a given time, once the process is complete, then the time is incremented forward and the process is repeated. The overall goal is to deliver solutions where the iterative error is controlled and the temporal discretization accuracy dictates the upper limit on the time step size (Δt^{lim}). Clearly, there are various combinations of solution methods that one can choose from. For example, for the overall field coupling, one may choose implicit or explicit staggering and within the staggering process, either implicit ($0 < \phi \leq 1$) or explicit time-stepping ($\phi = 0$), and, as mentioned previously in the case of implicit time-stepping, iterative or direct solvers for the balance of linear momentum and the first law of thermodynamics (Fig. 4).

3.5.1 Algorithmic Observation 1

It is important to emphasize that one should use the previous (converged) time step’s solution as the starting guess for the next time step to obtain a “head-start” ($\mathbf{u}^{K=0}(t + \Delta t) = \mathbf{u}(t)$). When selecting a time step, one must balance accuracy concerns and, simultaneously, stability issues.⁵ Clearly, the smaller the time-step, the more stable the solution process,

however, more time steps implies more system evaluations. Since the multifield staggering scheme iterates anyway, implicit methods are preferred for the applications of interest. As the physics changes, the field that is most sensitive (exhibits the largest amount of relative nondimensional change) dictates the time-step size. Because the internal system solvers within the staggering scheme are also iterative and use the previously converged solution as their starting value to solve the system of equations, a field that is relatively insensitive at given stage of the simulation will converge in a very few internal iterations (perhaps even one).

3.5.2 Algorithmic Observation 2

Generally speaking, the solution to the individual field equations progresses in a node by node fashion whereby, at a node (i, j, k) , for example for the mechanical field calculations, one has in an abstract form

$$\mathbf{u}(t + \Delta t) \approx \mathcal{F}(\mathbf{u}(t), \mathbf{u}(t + \Delta t), \theta(t), \theta(t + \Delta t)), \quad (3.47)$$

where the term on the lefthand side is updated and the terms on the right are previous iterate (old) values. This entails using the old values for all finite difference stencils that eventually become updated only after the algorithm completely traverse through the system, updating values, node by node (*no matrices need to be formed*, Fig. 4). There exist many methods to accelerate such computations, such as Successive Over-Relaxation, based on the pioneering work of Young [86]. For reviews, see Ames [1] or Axelsson [7]. Note that for the mechanical field calculations the thermal field is instantaneously fixed, and are updated only when it is to be solved, in the staggered manner (fixing the mechanical variables). At the algebraic equation solution level, after the individual field has been solved, the entire solution is passed to the next field equation, as described in the previous algorithm (Fig. 4). This is a Jacobi-type scheme, whereby the updates are made only after one complete system iteration, which is

⁵ Typically, the number of iterations needed to solve the coupled system, if an iterative scheme is used, increases with the time step size and the value of ϕ .

easier to address theoretically, as opposed to a Gauss-Seidel type method, which involves immediately using the most current field values, when they become available. The Jacobi method is easily parallelizable, if desired. In other words, the calculation for each node is (momentarily) uncoupled, with the updates only coming at the end of an iteration. Gauss-Seidel, since it requires the most current updates, couples the nodal calculations immediately.

4 A Specific Numerical Example-Controlled Heating

As mentioned at the outset of this paper, the specific manufacturing scenario that we are interested in modeling is a mixture which experiences laser-pulsing in targeted regions to induce a desired temperature field locally. This covers a wide range of applications in additive manufacturing. For illustration purposes, in this example, we control the lateral and side boundary conditions, set to be constant (thus laterally drawing heat out of the overall system). The top boundary is flux-type according to following: (a) if in the laser-zone

$$(\mathbf{K} \cdot \nabla \theta) \cdot \mathbf{n} = I \quad (4.1)$$

and (b) otherwise

$$(\mathbf{K} \cdot \nabla \theta) \cdot \mathbf{n} = 0. \quad (4.2)$$

In addition to the previously defined parameters, we have:

- Laser beam radius: $R_L = 0.1L = 0.00001$ m,
- Laser strength (W/m^2 , $I_o = 10^9$), where:

$$I(\mathbf{r}, t) = I_o e^{-c_o ||\mathbf{r} - \mathbf{r}_o||} \left((c_1 + c_2 \frac{t}{T}) (1 + \sin(2\pi\omega t/T)) \right), \quad (4.3)$$

and $\omega = 10 s^{-1}$, $c_o = 0$, $c_1 = 0$, $c_2 = 100$ and $T = 10^{-4}$.

- Absorption for the Beer-Lambert law:

$$I(\mathbf{r}, z, t) = I(\mathbf{r}, t) e^{-\int_0^{z^*} \alpha dz}, \quad (4.4)$$

where $\alpha = \alpha_1 e^{-\alpha_2 \frac{(\theta(x) - \theta_0)}{\theta_0}}$, for the matrix material: $\alpha_1 = 1$, $\alpha_2 = 0$ and for the particular material $\alpha_1 = 100$, $\alpha_2 = 0$.

As a model problem, we consider a group of particles with a smaller scale interstitial material that is assumed to be a continuous phase. We generated a group of N_p randomly dispersed spherical particles, of equal size, embedded in a cubical domain of dimensions, $D \times D \times D$. The particle size was determined by a particle/sample size ratio, which was defined via a subvolume size $V \stackrel{\text{def}}{=} \frac{D \times D \times D}{N_p}$. The non-dimensional ratio between the particle radii (b) and the subvolume was denoted by $\mathcal{L} \stackrel{\text{def}}{=} \frac{b}{V^{\frac{1}{3}}}$. The volume fraction

occupied by the particles can then be written as $v_p \stackrel{\text{def}}{=} \frac{4\pi\mathcal{L}^3}{3}$. Thus, the total volume occupied by the particles denoted ζ , can be written as $\zeta = v_p N_p V$. Large values of $\zeta > 0.5$ allow for overlap. We used $N_p = 100$ particles (Fig. 5). This sample size was determined by successively enlarging sample until there were no significant changes in the overall system response, for further enlargements. The classical random sequential addition algorithm was used to place nonoverlapping particles randomly into the domain of interest (RSA; Widom [85]). The particles were then enlarged from those locations and allowed to overlap.

Remark For higher volumes fractions, during the first phase of this algorithm (particle placement), more sophisticated algorithms, such as the equilibrium-based Metropolis algorithm can be used or methods based on simultaneous particle flow and growth, found in Torquato [81], Kansaal et. al [45] and Donev et. al [22, 23].

4.1 Sample Size Selection

In order to select a suitable sample that is statistically representative (a RVE), we employ a “framing” method, whereby the boundary conditions are applied (\mathbf{u} and θ) to the boundary of a sample (Fig. 5), and an interior subsample is used to probe what the material would experience without the direct influence of the applied boundary conditions. This approach avoids introducing boundary layer effects into the interior response. For more details, see Zohdi [89–103]. An implementation of a “framing” approach is as follows:

- *Step (1)* Generate a sample with a certain number of particles in its interior,
- *Step (2)* For the effective property calculation (averaging), select a subsample (“a sub-box”, Fig. 5) in the interior (to avoid boundary layer effects that arise from the imposition of boundary conditions),
- *Step (3)* Repeat Steps (1) and (2) for different random realizations for a given sample size, and average the resulting response to determine a mean value,
- *Step (4)* Repeat Steps (1)–(3) for a larger sample,
- *Step (5)* Continue the process [Steps (1)–(4)] until the response ceases to change to within an acceptable tolerance.

For a more in depth discussion on size-effect issues, see the works of Zohdi [89–103].

4.2 Numerical Examples

As an example, the following parameters were used:

- Reference temperature, $\theta_r = 300^\circ$ K,
- Initial temperature, $\theta_0 = 300^\circ$ K,
- Total time, $T = 10^{-5}$ s,

Fig. 5 Right With the framing method, a sample is probed with interior subsamples, within the larger sample, in order to avoid boundary layer effects that occur from imposing boundary conditions on the large-sample exterior. Left A mesh of the subsample

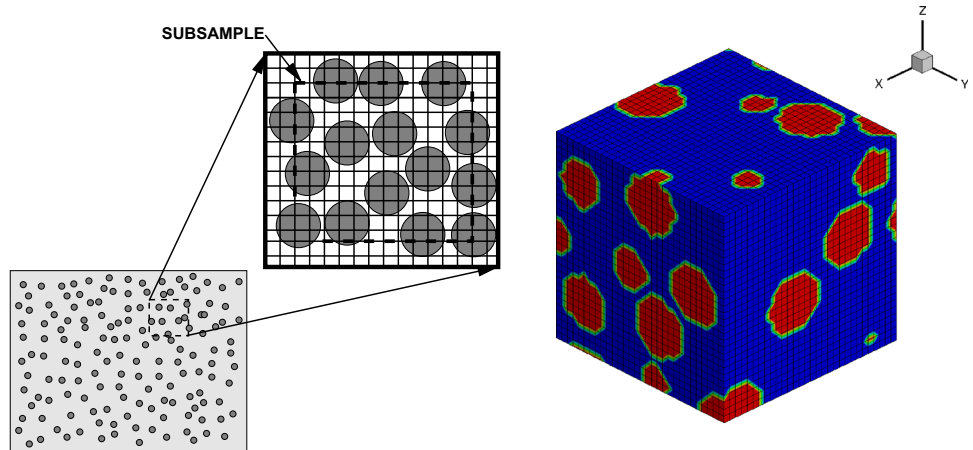
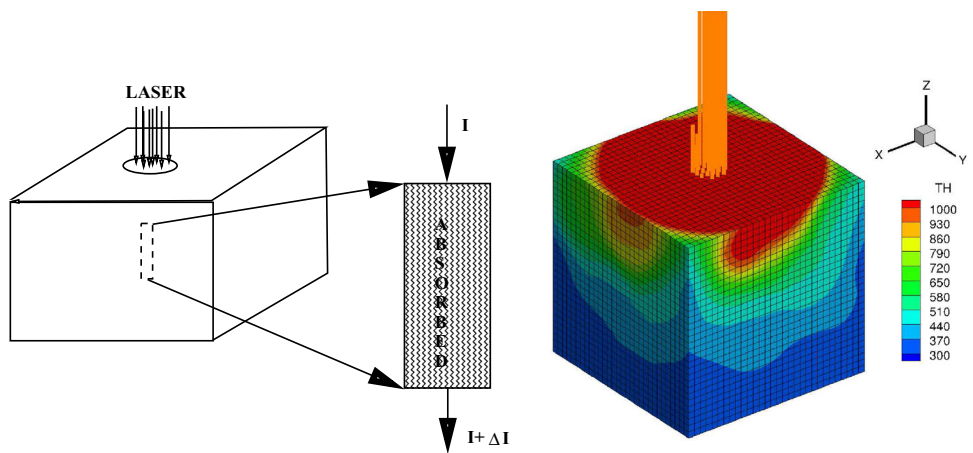


Fig. 6 Left Representations of laser input and absorption. Right Upcoming results showing mesh, absorption of energy and temperature



- Initial time step size, $\Delta t = 10^{-10}$ s,
- Damage lower bound, $\mathcal{D} = 0.1$,
- Displacement loading on all sides $\mathbf{u} = (0, 0, 0)$ m,
- Temperature of all sides (except top), $\theta(t) = 300^\circ$ K,
- Dimensions of the sample, $0.001 \times 0.001 \times 0.001$ m,
- Particles in the sample, $N_p = 100$,
- Base density, $\rho = 1000$ kg/m³,
- Base Lame parameters, $\lambda_o = 10$ Gpa, $\mu_o = 3$ Gpa,
- Base conductivity, $K_o = K_o \mathbf{1}$, $K_o = 100$ W/K-m,
- Base thermal expansion coefficient, $\beta_o = 0.000001$,
- Base heat capacity, $C_o = 10$ J/K-kg,
- Base plastic rate coefficient, $a_o = 0.001$,
- Base yield stress, $\sigma_{yo} = 10$ Mpa,
- Base damage rate coefficient, $b_o = -10000000$,
- Base damage flow stress, $\sigma_{do} = 10$ Mpa,
- Relative densities, $\rho_{1r} = \frac{\rho_1}{\rho} = 1$, $\rho_{2r} = \frac{\rho_2}{\rho} = 2$,
- Relative Lame parameters, $\lambda_{1r} = \frac{\lambda_1}{\lambda_o} = 5$, $\lambda_{2r} = \frac{\lambda_2}{\lambda_o} = 5$,
- Relative Lame parameters, $\mu_{1r} = \frac{\mu_1}{\mu_o} = 1$, $\mu_{2r} = \frac{\mu_2}{\mu_o} = 5$,
- Relative conductivity, $K_{1r} = \frac{K_1}{K_o} = 1$, $K_{2r} = \frac{K_2}{K_o} = 5$,

- Relative thermal expansion, $\beta_{1r} = \frac{\beta_1}{\beta_o} = 1$, $\beta_{2r} = \frac{\beta_2}{\beta_o} = 10$,
- Relative heat capacity, $C_{1r} = \frac{C_1}{C_o} = 1$, $C_{2r} = \frac{C_2}{C_o} = 2$,
- Relative plastic rate coefficient, $a_{1r} = \frac{a_1}{a_o} = 1$, $a_{2r} = \frac{a_2}{a_o} = 1$,
- Relative damage rate coefficient, $b_{1r} = \frac{b_1}{b_o} = 1$, $b_{2r} = \frac{b_2}{b_o} = 1$,
- Relative plastic yield, $\sigma_{y1r} = \frac{\sigma_{y1}}{\sigma_{yo}} = 1$, $\sigma_{y2r} = \frac{\sigma_{y2}}{\sigma_{yo}} = 5$,
- Relative damage threshold, $\sigma_{d1r} = \frac{\sigma_{d1}}{\sigma_{do}} = 1$, $\sigma_{d2r} = \frac{\sigma_{d2}}{\sigma_{do}} = 5$,
- A time stepping factor $\phi = 0.5$ (mid-point rule),
- An overlapping length scale of the particles of $\zeta = 0.375$,
- The number of desired iterations per time step set to $K_d = 5$, along with a coupling/staggering tolerance of $C_{tol} = 10^{-2}$,
- Weights for the iterative error norm, $w_1 = 0.5$ and $w_2 = 0.5$.

Throughout the computations, the spatial discretization meshes were repeatedly refined until the solutions did not exhibit any more sensitivity to further refinement of the grid-spacing.

4.3 Results

In Figs. 6, 7, 8, 9 and 10, frames of the sample and cross-sectional temperature profiles are shown for targeted laser heating. We started with meshes such as a $21 \times 21 \times 21$ mesh, arising from having a cubical mesh with 10 nodes from the centerline plane of symmetry and one node in the middle, and then repeatedly refined in the following sequential manner:

1. **Mesh # 1:** a $21 \times 21 \times 21$ mesh, which has 9,261 degrees of freedom (DOF) for the thermal field and 27,783 DOF for the mechanical field, for a total of 37,044 DOF.
2. **Mesh # 2:** a $41 \times 41 \times 41$ mesh, which has 68921 degrees of freedom (DOF) for the thermal field and 206783 DOF for the mechanical field, for a total of 275,684 DOF.
3. **Mesh # 3:** a $61 \times 61 \times 61$ mesh, which has 226,981 degrees of freedom (DOF) for the thermal field and 680,943 DOF for the mechanical field, for a total of 907,924 DOF.
4. **Mesh # 4:** a $81 \times 81 \times 81$ mesh, which has 531,441 degrees of freedom (DOF) for the thermal field and 1,594,322 DOF for the mechanical field, for a total of 2,125,764 DOF.

Approximately between a 61-level and a 81-level mesh, the results stabilized, indicating that the results are essentially free of any appreciable numerical error. At the length-scales of interest, it is questionable whether the ideas of a sharp material interface are justified. Accordingly, we simulated the system with and without Laplacian smoothing, whereby one smooths the material data by post-processing the material data, node by node, to produce a smoother material representation, for example, for the thermal conductivity, $\hat{\mathbb{K}}$ (using the stencil in Fig. 11 in the “Appendix 1”)

$$\nabla_x^2 \mathbb{K} = \mathbf{0} \Rightarrow \hat{\mathbb{K}}_{i,j,k} = \frac{1}{6} (\mathbb{K}_{i+1,j,k} + \mathbb{K}_{i-1,j,k} + \mathbb{K}_{i,j+1,k} + \mathbb{K}_{i,j-1,k} + \mathbb{K}_{i,j,k+1} + \mathbb{K}_{i,j,k-1}). \quad (4.5)$$

The same was done for the mechanical properties by enforcing $\nabla_x^2 \lambda_0 = \mathbf{0}$ and $\nabla_x^2 \mu_0 = \mathbf{0}$ and as well as other material data. The simulations were run with and without data smoothing, with the results being negligibly different for sufficiently fine meshes. The size of the time steps were

purposely started quite small ($\Delta t = 10^{-10}$ seconds) and given an enlargement cap of 50 times in magnitude. This allows the system to slowly evolve to capture the quite transient behavior. During the bulk of the computation, the large steps were warranted (the time-step size evolved), as dictated by the physics and the adaptive algorithm. For other material selections and loading regimes, other adaptivity modes can occur. All simulations were run on a standard laptop requiring minimal memory requirements. It is important to stress that it is virtually impossible to determine a-priori whether the initial time step is adequate to meet a tolerance and whether adaptivity is needed. *Obviously, we can use this scheme for any (trapezoidal) value of $0 \leq \phi \leq 1$.* Time-step size adaptivity is important, since the solution can dramatically change over the course of time, possibly requiring quite different time step sizes to control the iterative (staggering) error. However, to maintain the accuracy of the time-stepping scheme, one must respect an upper bound dictated by the discretization error, i.e., $\Delta t \leq \Delta t^{lim}$. The example shown was simply to illustrate the overall process. The simulation of targeted heating is a subject of current research by the author, extending this model to include phase transformations involving melting and vaporization and the debris ejecta, which involves multiple stages of nonmonotone evaporative heating and cooling, and mass transfer.

Remark While our stated focus is the evolution of stresses, a by-product of the analysis overall effective mechanical stiffness relation defined by

$$\langle \boldsymbol{\sigma} \rangle_\Omega = \mathcal{F}^*(\langle \boldsymbol{\epsilon} \rangle_\Omega), \quad (4.6)$$

where $\langle \cdot \rangle_\Omega \stackrel{\text{def}}{=} \frac{1}{|\Omega|} \int_\Omega \cdot d\Omega$. Similarly, one can generate effective thermal responses

$$\langle \boldsymbol{q} \rangle_\Omega = \mathcal{G}^*(\langle \nabla \theta \rangle_\Omega). \quad (4.7)$$

There are a variety of estimates for effective responses in many fields. We refer the reader to Hashin and Shtrikman [33] based on variational principles using the concept of polarization tensor fields (filtering/separation of micro-macro scales) and numerical techniques to extract the effective response of such materials (Zohdi [89–103]). Estimates for the effective properties of heterogeneous materials date back over 150 years to Maxwell [55] and [56] and Lord Rayleigh [69]. For a relatively recent and thorough analysis of a variety of classical approaches, such as the ones briefly mentioned here, see Torquato [81] for general interdisciplinary discussions, Jikov et al. [40] for more mathematical aspects, Hashin [34], Mura [57], Nemat-Nasser and Hori [61] for solid-mechanics inclined accounts of the subject, for analyses of defect-laden, porous and cracked media, see Kachanov [42], Kachanov,

Fig. 7 From left to right and top to bottom: the temperature (in Kelvin), with pulsed laser input. The morphology is shown in Fig. 5

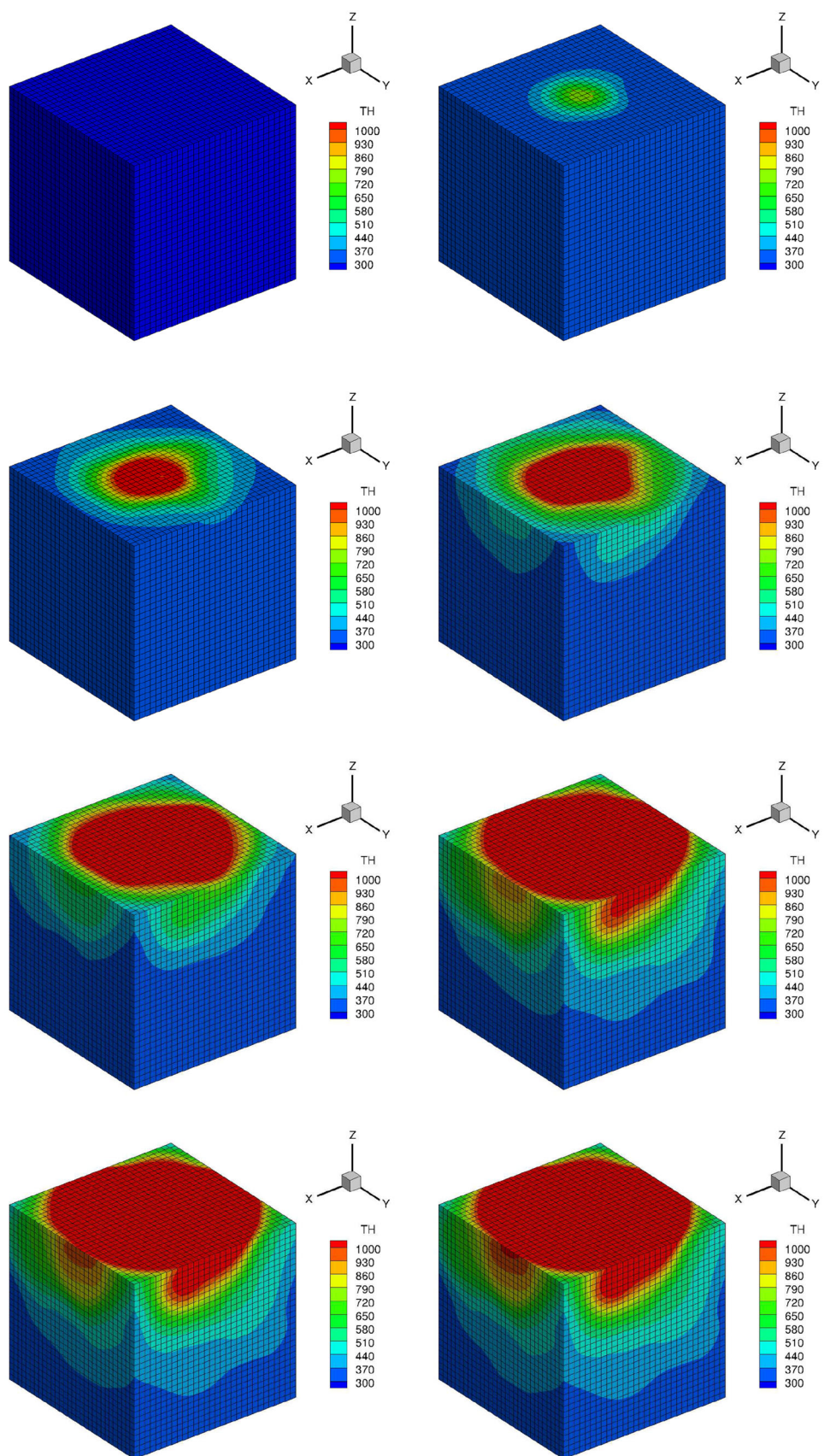


Fig. 8 From left to right and top to bottom: orthogonal slices through the microstructure for the temperature (in Kelvin), with pulsed laser input

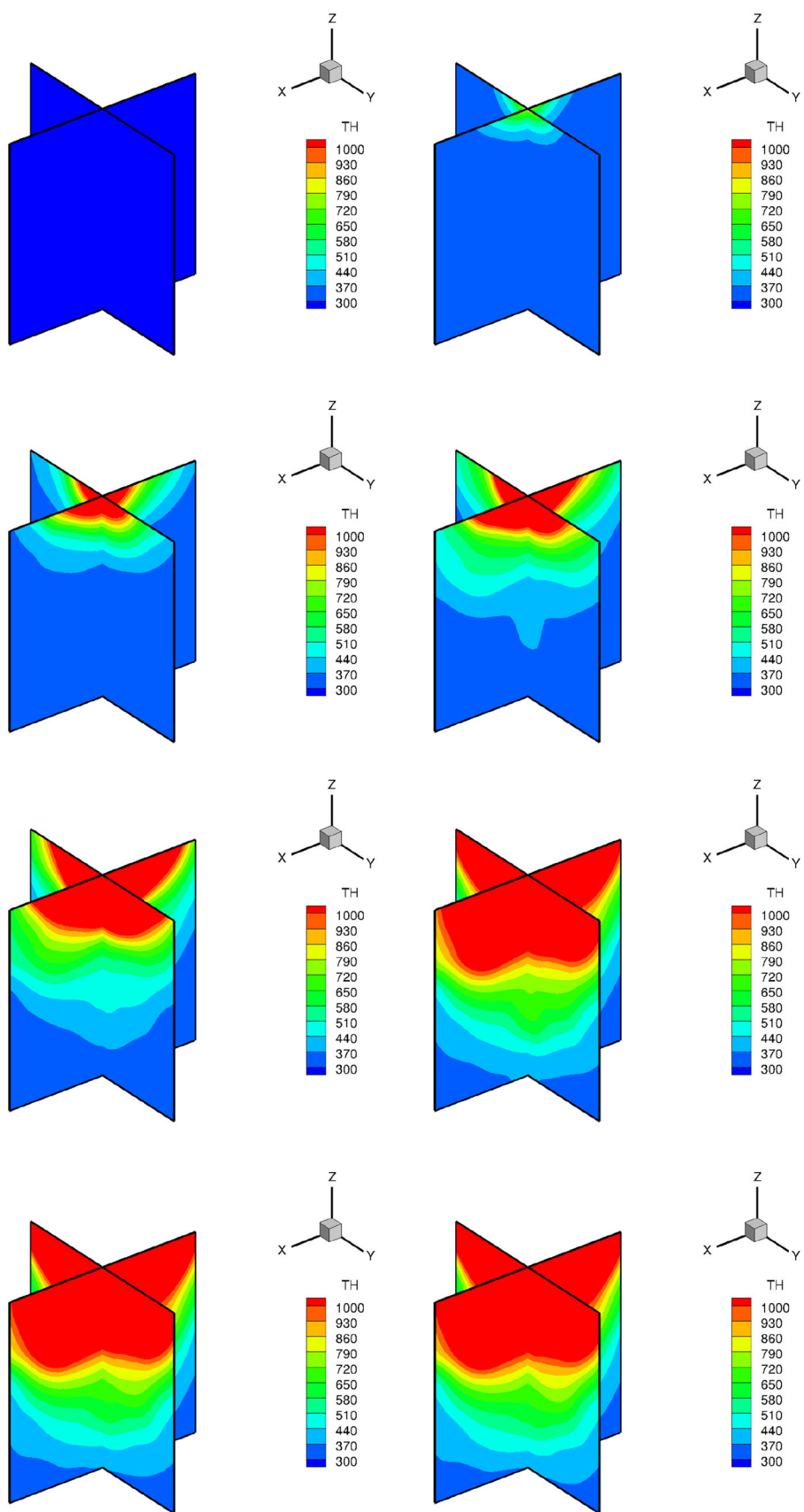


Fig. 9 From left to right and top to bottom: the norm of the deviatoric stress (in GPa), with pulsed laser input

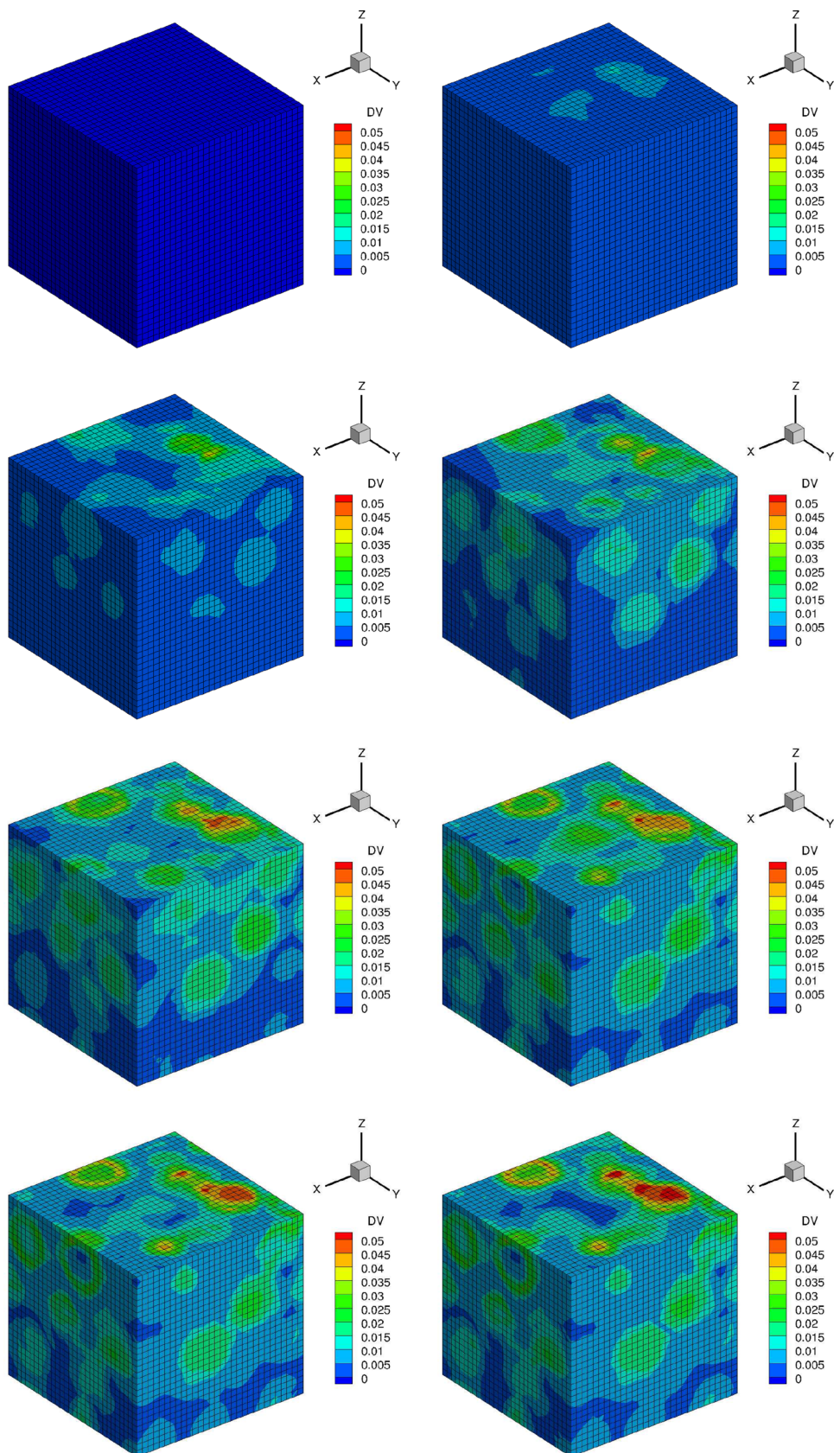


Fig. 10 From left to right and top to bottom: orthogonal slices through the microstructure—the norm of the deviatoric stress (in GPa), with pulsed laser input

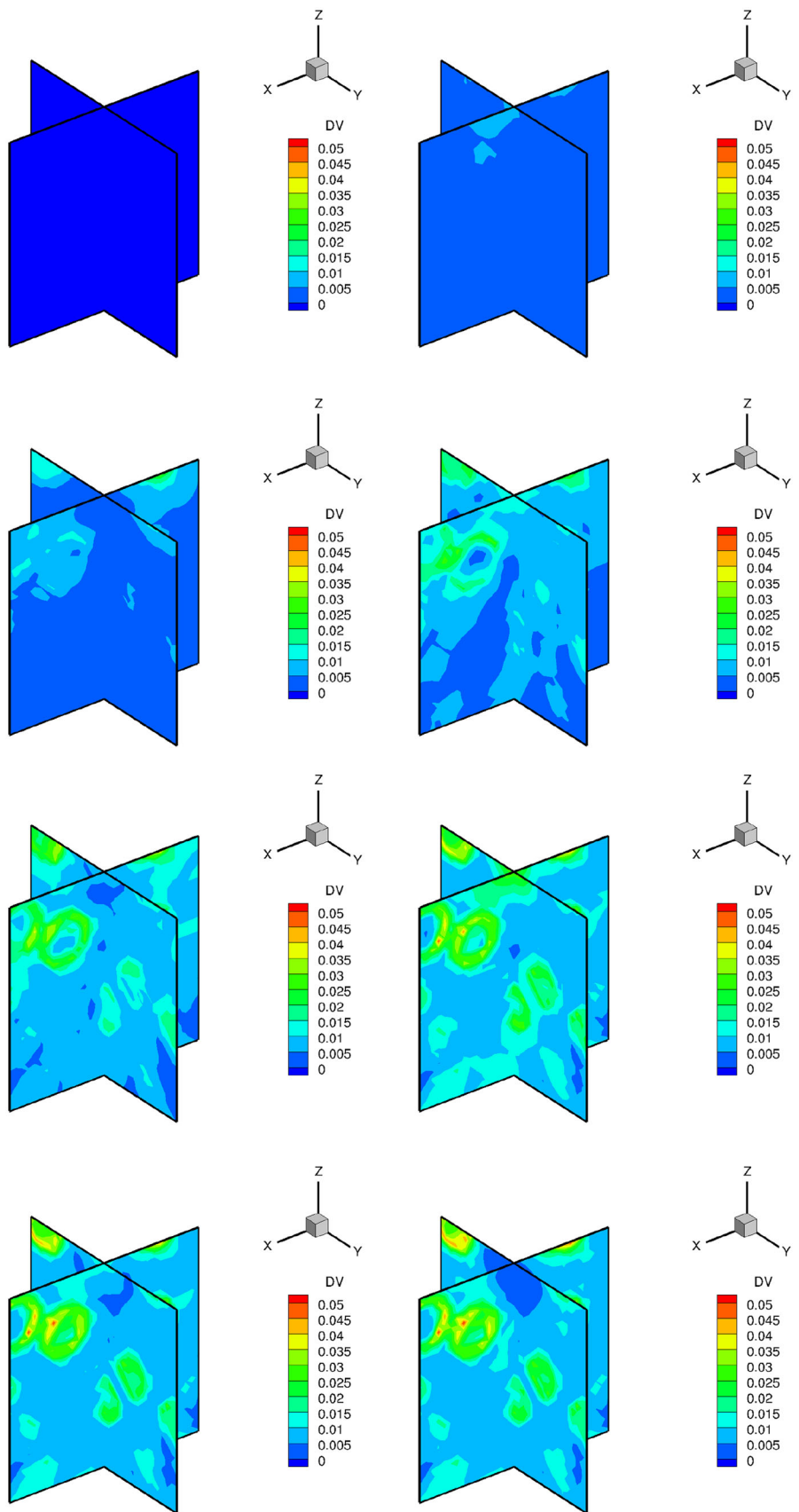
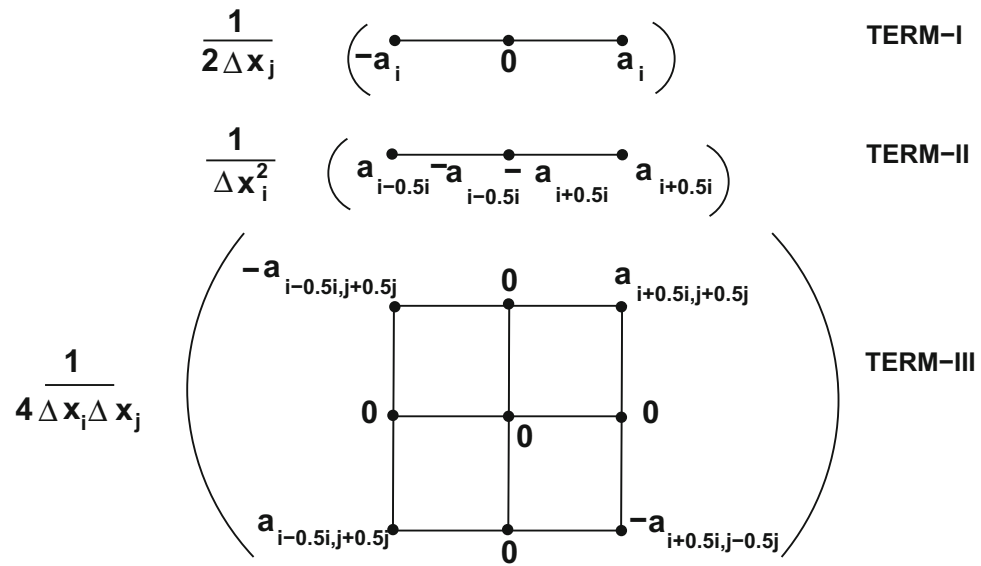


Fig. 11 Various Finite-difference stencils in “computational molecule” form (centered at (x_i, x_j, x_k)), where: (1) TERM-I: $a \frac{\partial u}{\partial x_i}$, (2) TERM-II: $\frac{1}{\Delta x_i} \left(a \frac{\partial u}{\partial x_i} \right)$ and (3) TERM-III: $\frac{1}{4 \Delta x_i \Delta x_j} \left(a \frac{\partial u}{\partial x_i} \right)$, following Zohdi [89–103]



Tsukrov and Shafiro [43], Kachanov and Sevostianov [44], Sevostianov, Gorbatikh and Kachanov [77], Sevostianov and Kachanov [78], and for computational aspects see Ghosh [30], Ghosh and Dimiduk [31] and Zohdi [89–103]

4.4 Extensions: Advanced Models for Conduction Utilizing Thermal Relaxation

Within the last decade, technological advances have enabled the reliable control of ultrafast pulsed lasers to activate small-time scale heat wave effects. These effects are often referred to as thermally-relaxed “second-sound” effects, because of their mathematical similarity to wave propagation in acoustics, although normal sound waves are fluctuations in the density of molecules in a substance while thermally-relaxed second-sound waves are fluctuations in the density of phonons. Such phenomena are predicted by models which introduce thermal relaxation times into heat-conduction relations. The thermally-relaxed second-sound is a quantum mechanical phenomenon in which heat transfer occurs by wave-like motion, rather than by the more usual mechanism of diffusion. This leads to a very high confinement of thermal energy in very targeted zones. Thermally-relaxed phenomena can be observed in any system in which most phonon–phonon collisions conserve momentum, and can play a role when the time scale of heat input is quite small.

4.4.1 Thermally-Relaxed Continuum Model

The thermally-relaxed second-sound type model can be motivated by a Jeffreys-type relation between the

conductive flux and temperature gradient (Joseph and Preziosi [66] and Ignaczak and Ostoja-Starzewski [39]):

$$\tau \frac{\partial \mathbf{q}_k}{\partial t} + \mathbf{q}_k = -\mathcal{K} \cdot \nabla \theta, \quad (4.8)$$

where τ is the relaxation time, θ is the temperature, t is time, \mathbf{q}_k is the conductive heat flux, \mathcal{K} is the thermal conductivity. To clearly illustrate the character of this model, relative to standard heat conduction, we ignore stress-power effects, yielding

$$\rho C \frac{\partial \theta}{\partial t} = -\nabla \cdot \mathbf{q}_k + \mathcal{S}, \quad (4.9)$$

where ρ is the mass density, C is the heat capacity and \mathcal{S} represents other sources, such as laser energy input. By taking the partial derivative with respect to time of the above yields, assuming no material changes,

$$\rho C \frac{\partial^2 \theta}{\partial t^2} = -\frac{\partial \nabla \cdot \mathbf{q}_k}{\partial t} + \frac{\partial \mathcal{S}}{\partial t} = -\nabla \cdot \frac{\partial \mathbf{q}_k}{\partial t} + \frac{\partial \mathcal{S}}{\partial t}. \quad (4.10)$$

Inserting Eqs. 4.8 into 4.9 and 4.10 yields

$$\frac{\partial^2 \theta}{\partial t^2} + \frac{1}{\tau} \frac{\partial \theta}{\partial t} = \frac{1}{\rho C \tau} \nabla \cdot (\mathcal{K} \cdot \nabla \theta) + \frac{1}{\rho C \tau} \mathcal{S} + \frac{1}{\rho C} \frac{\partial \mathcal{S}}{\partial t}. \quad (4.11)$$

This produces attenuating heat waves. In the case of a homogeneous medium, the wave speed is $\sqrt{\frac{\mathcal{K}}{\rho C \tau}}$.

4.4.2 Extreme Cases

We have the following extreme parameter cases:

- In the special case of $\tau \rightarrow 0$, one obtains the classical heat conduction equation

$$\rho C \frac{\partial \theta}{\partial t} = \nabla \cdot \mathbf{K} \cdot \nabla \theta + \mathcal{S}. \quad (4.12)$$

- In the special case of $\tau \rightarrow \infty$, one obtains

$$\rho C \frac{\partial^2 \theta}{\partial t^2} = \frac{\partial \mathcal{S}}{\partial t} \Rightarrow \rho C \frac{\partial \theta}{\partial t} = \mathcal{S}, \quad (4.13)$$

which eliminates heat losses due to conduction, thus confining heat input.

- In the special case when $\tau \rightarrow \infty$, $\mathbf{K} \rightarrow \infty$ and $\frac{\mathbf{K}}{\tau}$ remaining finite, then a purely hyperbolic equation arises

$$\frac{\partial^2 \theta}{\partial t^2} = \frac{1}{\rho C \tau} \nabla \cdot \mathbf{K} \cdot \nabla \theta. \quad (4.14)$$

An excellent review of a wide range of heat transfer models can be found in the seminal review paper of Joseph and Preziosi [66] or the text of Ignaczak and Ostoja-Starzewski [39]. In the general case, we couple Eq. 4.8 to the more general First Law:

$$\rho \dot{w} = \boldsymbol{\sigma} : \nabla \dot{\mathbf{u}} - \nabla \cdot \mathbf{q}_k + \rho z. \quad (4.15)$$

4.4.3 Algorithm for Thermal Relaxation

The thermally-relaxed heat flux, since it is governed by its own PDE, requires simultaneous solution with the other governing equations. We approach this from a staggering point of view by, at a time-step, at every node in the system:

- Solve for \mathbf{q} fixing θ ,
- Solve for θ (using the just updated \mathbf{q}) and
- Repeating until convergence.

At each iteration, \mathbf{q} can be solved for analytically (for fixed θ). We proceed by solving the following ODE (spatially fixed), for each component $\mathbf{q} = (q_1, q_2, q_3)$, over the interval $t_o \leq t \leq t_o + \phi \Delta t$

$$\tau \frac{\partial q_i}{\partial t} + q_i = -(\mathbf{K} \cdot \nabla \theta)_i \quad (4.16)$$

with initial condition $q_i = q_i(t = t_o)$. Since we are “freezing” θ , this yields an ODE in time with solution (defining $\tilde{t} = t - t_o$)

$$q_i(\tilde{t}) = \underbrace{(q_i(\tilde{t}=0) + (\mathbf{K} \cdot \nabla \theta(\tilde{t}+t_o))_i)}_{\text{slows conduction}} e^{-\frac{\tilde{t}}{\tau}} - \underbrace{(\mathbf{K} \cdot \nabla \theta(\tilde{t}+t_o))_i}_{\text{regular conduction}}, \quad (4.17)$$

which yields at time t

$$\mathbf{q}(t) = \underbrace{(\mathbf{q}(t_o) + (\mathbf{K} \cdot \nabla \theta(t)))e^{-\frac{t-t_o}{\tau}}}_{\text{slows conduction}} - \underbrace{(\mathbf{K} \cdot \nabla \theta(t))}_{\text{regular conduction}}, \quad (4.18)$$

For the spatial discretization (needed in the First Law of Thermodynamics) this yields:

$$\begin{aligned} \nabla \cdot \mathbf{q} &= \nabla \cdot (\mathbf{q}(t_o) + (\mathbf{K} \cdot \nabla \theta(t_o + \phi \Delta t)))e^{-\frac{t-t_o}{\tau}} \\ &\quad + (\mathbf{q}(t_o) + (\mathbf{K} \cdot \nabla \theta(t_o + \phi \Delta t))) \cdot \nabla e^{-\frac{t-t_o}{\tau}} \\ &\quad - \nabla \cdot (\mathbf{K} \cdot \nabla \theta(t_o + \phi \Delta t)), \end{aligned} \quad (4.19)$$

where

$$\nabla e^{-\frac{t-t_o}{\tau}} = (t - t_o) \tau^{-2} e^{-\frac{t-t_o}{\tau}} \nabla \tau. \quad (4.20)$$

Remark 1 This yields at time $t = t_o + \phi \Delta t$

$$\begin{aligned} \mathbf{q}(t_o + \phi \Delta t) &= \underbrace{(\mathbf{q}(t_o) + (\mathbf{K} \cdot \nabla \theta(t_o + \phi \Delta t)))e^{-\frac{\phi \Delta t}{\tau}}}_{\text{slows conduction}} \\ &\quad - \underbrace{(\mathbf{K} \cdot \nabla \theta(t_o + \phi \Delta t))}_{\text{regular conduction}}, \end{aligned} \quad (4.21)$$

which is needed in the trapezoidal time stepping scheme.

Remark 2 We note that for a Discrete Element Method formulation,

$$m_i C_i \dot{\theta}_i = -\mathbf{q}_i \cdot \mathbf{n}_i A_i = q_i^* A_i \quad (4.22)$$

this becomes⁶

$$\begin{aligned} q_i^*(t)_i &= -\left(\mathbf{q}(t_o) + \left(\mathbf{K}_i \frac{\theta_j - \theta_i}{\|\mathbf{r}_j - \mathbf{r}_i\|} \right) \Big|_{t_o} \right) e^{-\frac{t-t_o}{\tau}} \\ &\quad + \left(\mathbf{K}_i \frac{\theta_j - \theta_i}{\|\mathbf{r}_j - \mathbf{r}_i\|} \right) \Big|_{t_o}. \end{aligned} \quad (4.24)$$

5 Summary and Extensions

The spatial discretization grids used were uniform and dense, and the deposited microstructure was embedded into spatial discretization. The regular grid allows one to generate a matrix-free iterative formulation which is amenable to rapid calculation and minimal memory requirements, making it ideal for laptop computation. From the point of view of computational challenges, the types of numerical methods needed to simulate such processes are still in their infancy. What was illustrated in this paper was the analysis on one isolated component of an overall additive process—namely the subprocess of laser energy input. There are many more related process which must be coupled to this

⁶ For example, for a trapezoidal time-stepping scheme

$$\begin{aligned} q_i^*(t_o + \phi \Delta t)_i &= -\left(\mathbf{q}(t_o) + \left(\mathbf{K}_i \frac{\theta_j - \theta_i}{\|\mathbf{r}_j - \mathbf{r}_i\|} \right) \Big|_{t_o+\phi \Delta t} \right) e^{-\frac{\phi \Delta t}{\tau}} \\ &\quad + \left(\mathbf{K}_i \frac{\theta_j - \theta_i}{\|\mathbf{r}_j - \mathbf{r}_i\|} \right) \Big|_{t_o+\phi \Delta t}. \end{aligned} \quad (4.23)$$

subprocess. One objective of future research is the development of Discrete Element models for the dynamics of deposition, which can be seamlessly coupled to continuum-based models, utilizing the best of both formulations, that capture the following main physical events:

- particle motion/dynamics, which primarily entails: (a) the movement of the particles induced by contact with substrates (which are potentially electrified) and (b) particle-to-particle contact forces,
- particle electrical current flow, which primarily entails: (a) current flow through the particles and (b) current exchange between the particles and walls,
- particle thermodynamics, which primarily entails: (a) heat transfer between particles in contact by conduction, (b) thermal softening of the particles and (c) change of phase from a solid, to a liquid to a gas,
- discretization of laser beams (or other external heat sources, such as e-beams, infra-red sources, etc) and models which track such energy propagation (such as optical reflection and absorption) through complex material microstructure, its conversion into heat and the subsequent conduction and phase transformations involving melting and vaporization,
- Modeling and simulation potentially hazardous debris (sublimated) ejecta from laser ablation of substrates or deposited materials, employing a combination of discrete element and continuum methods.

Any realistic simulation of an advanced additive manufacturing process will involve many of the subprocesses mentioned above, leading to a strongly-coupled multiphysical system, since the dynamics controls which particles are in mechanical contact, thus dictating the possible electrical contacts and conduction, which in turn controls the conductive heating and softening and binding the material, as well as the interaction with external laser-based sources, as seen in this monograph. For example, approaches taken here are to construct a submodel for each primary physical process mentioned above. These submodels are coupled to one another and are solved by extending the recursive multiphysical staggering scheme, as discussed in this paper. The modular approach allows for easy improvement, replacement or addition to submodels, if needed. For more details, the reader is referred to Zohdi [89–103]. Variants of the technique have been applied to related problems involving more coupled multiphysics, such as electro-magneto-thermo-mechano-chemo effects, in Zohdi [89–103], whereby one computes the electrical \mathbf{E} -field with the magnetic field \mathbf{H} , thermal field θ , displacement field \mathbf{u} and chemical field c fixed, then computes \mathbf{H} -field with \mathbf{E} , θ , \mathbf{u} and c fields fixed, etc, and iterates at time interval $L + 1$, $K = 1, 2, \dots$ for (written directly in iterative implicit form)

$$\underline{\mathbf{E}}^{L+1,K} = \mathcal{F}(\underline{\mathbf{E}}^{L+1,K-1}, \underline{\mathbf{H}}^{L+1,K-1}, \underline{\theta}^{L+1,K-1}, \underline{\mathbf{u}}^{L+1,K-1}, \underline{c}^{L+1,K-1}), \quad (5.1)$$

and

$$\underline{\mathbf{H}}^{L+1,K} = \mathcal{G}(\underline{\mathbf{E}}^{L+1,K}, \underline{\mathbf{H}}^{L+1,K-1}, \underline{\theta}^{L+1,K-1}, \underline{\mathbf{u}}^{L+1,K-1}, \underline{c}^{L+1,K-1}), \quad (5.2)$$

and

$$\underline{\theta}^{L+1,K} = \mathcal{Y}(\underline{\mathbf{E}}^{L+1,K}, \underline{\mathbf{H}}^{L+1,K}, \underline{\theta}^{L+1,K-1}, \underline{\mathbf{u}}^{L+1,K-1}, \underline{c}^{L+1,K-1}), \quad (5.3)$$

and

$$\underline{\mathbf{u}}^{L+1,K} = \mathcal{L}(\underline{\mathbf{E}}^{L+1,K}, \underline{\mathbf{H}}^{L+1,K}, \underline{\theta}^{L+1,K}, \underline{\mathbf{u}}^{L+1,K-1}, \underline{c}^{L+1,K-1}), \quad (5.4)$$

and

$$\underline{c}^{L+1,K} = \mathcal{C}(\underline{\mathbf{E}}^{L+1,K}, \underline{\mathbf{H}}^{L+1,K}, \underline{\theta}^{L+1,K}, \underline{\mathbf{u}}^{L+1,K}, \underline{c}^{L+1,K-1}), \quad (5.5)$$

where the only underlined variable is active at that stage of the process. One then computes the maximum of the error measures $\varpi^{*,K} \stackrel{\text{def}}{=} \max(\varpi_E^K, \varpi_H^K, \varpi_\theta^K, \varpi_u^K, \varpi_c^K)$ in order to determine if time-step adaptivity is necessary, as introduced earlier for the thermo-mechanical scheme. Generally, the methods discussed in this work can be combined to create hybrid block-partitioned approaches, whereby the entire domain is partitioned into subdomains and within each subdomain an iterative method is applied. In other words, for a subdomain, the values at all nodes from outside are initially frozen, as far as calculations involving members of the group are concerned. After each isolated subdomain's solution (nodal values) has converged (computed in parallel), then all nodal values are updated, i.e. the most current values become available to all members of the grid, and the isolated subdomain calculations are repeated. Although parallel computation of the introduced algorithms was not pursued in this work, it is currently being investigated by the author.

Acknowledgments This work was funded in part by the Army Research Laboratory through the Army High Performance Computing Research Center (cooperative agreement W911NF-07-2-0027).

Appendix 1: Spatial Finite Difference Stencils

Following Zohdi [89–103], standard approximations are used:

1. For the first derivative of a primal variable u at (x_1, x_2, x_3) :

$$\frac{\partial u}{\partial x_1} \approx \frac{u(x_1 + \Delta x_1, x_2, x_3) - u(x_1 - \Delta x_1, x_2, x_3)}{2\Delta x_1} \quad (6.1)$$

2. For the derivative of a flux at (x_1, x_2, x_3) , with an arbitrary material coefficient a :

$$\begin{aligned} \frac{\partial}{\partial x_1} \left(a \frac{\partial u}{\partial x_1} \right) &\approx \frac{\left(a \frac{\partial u}{\partial x_1} \right) \Big|_{x_1+\frac{\Delta x_1}{2}, x_2, x_3} - \left(a \frac{\partial u}{\partial x_1} \right) \Big|_{x_1-\frac{\Delta x_1}{2}, x_2, x_3}}{\Delta x_1} \\ &= \frac{1}{\Delta x_1} \left[a(x_1 + \frac{\Delta x_1}{2}, x_2, x_3) \right. \\ &\quad \times \left(\frac{u(x_1 + \Delta x_1, x_2, x_3) - u(x_1, x_2, x_3)}{\Delta x_1} \right) \\ &\quad - \frac{1}{\Delta x_1} \left[a(x_1 - \frac{\Delta x_1}{2}, x_2, x_3) \right. \\ &\quad \times \left. \left(\frac{u(x_1, x_2, x_3) - u(x_1 - \Delta x_1, x_2, x_3)}{\Delta x_1} \right) \right], \end{aligned} \quad (6.2)$$

where we have used

$$a(x_1 + \frac{\Delta x_1}{2}, x_2, x_3) \approx \frac{1}{2}(a(x_1 + \Delta x_1, x_2, x_3) + a(x_1, x_2, x_3)) \quad (6.3)$$

and

$$\begin{aligned} a(x_1 - \frac{\Delta x_1}{2}, x_2, x_3) &\approx \frac{1}{2} \left(a(x_1, x_2, x_3) \right. \\ &\quad \left. + a(x_1 - \Delta x_1, x_2, x_3) \right) \end{aligned} \quad (6.4)$$

3. For the cross-derivative of a flux at (x_1, x_2) :

$$\begin{aligned} \frac{\partial}{\partial x_2} \left(a \frac{\partial u}{\partial x_1} \right) &\approx \\ &\quad \times \left(\frac{u(x_1 + \Delta x_1, x_2, x_3) - u(x_1 - \Delta x_1, x_2, x_3)}{2\Delta x_1} \right) \\ &\approx \frac{1}{4\Delta x_1 \Delta x_2} (a(x_1, x_2 + \Delta x_2, x_3) \\ &\quad \times [u(x_1 + \Delta x_1, x_2 + \Delta x_2, x_3) \\ &\quad - u(x_1 - \Delta x_1, x_2 + \Delta x_2, x_3)] \\ &\quad - a(x_1, x_2 - \Delta x_2, x_3) [u(x_1 + \Delta x_1, x_2 \\ &\quad - \Delta x_2, x_3) - u(x_1 - \Delta x_1, x_2 - \Delta x_2, x_3)]), \end{aligned} \quad (6.5)$$

Remark To illustrate second-order accuracy, consider a Taylor series expansion for an arbitrary function u

$$\begin{aligned} u(x + \Delta x) &= u(x) + \frac{\partial u}{\partial x} \Big|_x \Delta x + \frac{1}{2} \frac{\partial^2 u}{\partial x^2} \Big|_x (\Delta x)^2 \\ &\quad + \frac{1}{6} \frac{\partial^3 u}{\partial x^3} \Big|_x (\Delta x)^3 + \mathcal{O}((\Delta x)^4) \end{aligned} \quad (6.6)$$

and

$$\begin{aligned} u(x - \Delta x) &= u(x) - \frac{\partial u}{\partial x} \Big|_x \Delta x + \frac{1}{2} \frac{\partial^2 u}{\partial x^2} \Big|_x (\Delta x)^2 \\ &\quad - \frac{1}{6} \frac{\partial^3 u}{\partial x^3} \Big|_x (\Delta x)^3 + \mathcal{O}((\Delta x)^4) \end{aligned} \quad (6.7)$$

Subtracting the two expressions yields

$$\frac{\partial u}{\partial x} \Big|_x = \frac{u(x + \Delta x) - u(x - \Delta x)}{2\Delta x} + \mathcal{O}((\Delta x)^2). \quad (6.8)$$

Appendix 2: Temporally-Adaptive Iterative Methods

Implicit time-stepping methods, with time step size adaptivity, built on approaches found in Zohdi [89–103] were used throughout the analysis in the body of the work. In order to introduce basic concepts, we consider a first order differential equation for a field \mathbf{W} :

$$\dot{\mathbf{W}} = \Lambda(\mathbf{W}), \quad (7.1)$$

which, after being discretized using a trapezoidal “ ϕ -method” ($0 \leq \phi \leq 1$)

$$\mathbf{W}^{L+1} = \mathbf{W}^L + \Delta t (\phi \Lambda(\mathbf{W}^{L+1}) + (1 - \phi) \Lambda(\mathbf{W}^L)). \quad (7.2)$$

Generally, for systems of equations of this form, a straightforward iterative scheme can be written as

$$\mathbf{W}^{L+1,K} = \mathcal{G}(\mathbf{W}^{L+1,K-1}) + \mathcal{R}, \quad (7.3)$$

where \mathcal{R} is a remainder term that does not depend on the solution, i.e. $\mathcal{R} \neq \mathcal{R}(\mathbf{W}^{L+1})$, and $K = 1, 2, 3, \dots$ is the index of iteration within time step $L + 1$. The convergence of such a scheme is dependent on the behavior of \mathcal{G} . Namely, a sufficient condition for convergence is that \mathcal{G} is a contraction mapping for all $\mathbf{W}^{L+1,K}$, $K = 1, 2, 3, \dots$. In order to investigate this further, we define the iteration error as

$$\varpi^{L+1,K} \stackrel{\text{def}}{=} \|\mathbf{W}^{L+1,K} - \mathbf{W}^{L+1}\|. \quad (7.4)$$

A necessary restriction for convergence is iterative self consistency, i.e. the “exact” (discretized) solution must be represented by the scheme

$$\mathcal{G}(\mathbf{W}^{L+1}) + \mathcal{R} = \mathbf{W}^{L+1}. \quad (7.5)$$

Enforcing this restriction, a sufficient condition for convergence is the existence of a contraction mapping

$$\varpi^{L+1,K} = \|\mathbf{W}^{L+1,K} - \mathbf{W}^{L+1}\| = \|\mathcal{G}(\mathbf{W}^{L+1,K-1}) - \mathcal{G}(\mathbf{W}^{L+1})\| \quad (7.6)$$

$$\leq \eta^{L+1,K} \|\mathbf{W}^{L+1,K-1} - \mathbf{W}^{L+1}\|, \quad (7.7)$$

where, if $0 \leq \eta^{L+1,K} < 1$ for each iteration K , then $\varpi^{L+1,K} \rightarrow 0$ for any arbitrary starting value $\mathbf{W}^{L+1,K=0}$, as $K \rightarrow \infty$. This type of contraction condition is sufficient, but not necessary, for convergence. Inserting these approximations into $\dot{\mathbf{W}} = \boldsymbol{\Lambda}(\mathbf{W})$ leads to

$$\mathbf{W}^{L+1,K} \approx \underbrace{\Delta t (\phi \boldsymbol{\Lambda}(\mathbf{W}^{L+1,K-1}))}_{\mathcal{G}(\mathbf{W}^{L+1,K-1})} + \underbrace{\Delta t (1-\phi) \boldsymbol{\Lambda}(\mathbf{W}^L) + \mathbf{W}^L}_{\mathcal{R}} \quad (7.8)$$

whose contraction constant is scaled by $\eta \propto \phi \Delta t$. Therefore, if convergence is slow within a time step, the time step size, which is adjustable, can be reduced by an appropriate amount to increase the rate of convergence. Decreasing the time step size improves the convergence, however, we want to simultaneously maximize the time-step sizes to decrease overall computing time, while still meeting an error tolerance on the numerical solution's accuracy. In order to achieve this goal, we follow an approach found in Zohdi [89–103] originally developed for continuum thermo-chemical multifield problems in which one first approximates

$$\eta^{L+1,K} \approx S(\Delta t)^p \quad (7.9)$$

(S is a constant) and secondly one assumes the error within an iteration to behave according to

$$(S(\Delta t)^p)^K \varpi^{L+1,0} = \varpi^{L+1,K}, \quad (7.10)$$

$K = 1, 2, \dots$, where $\varpi^{L+1,0}$ is the initial norm of the iterative error and S is intrinsic to the system.⁷ Our goal is to meet an error tolerance in exactly a preset number of iterations. To this end, one writes

$$(S(\Delta t_{\text{tol}})^p)^{K_d} \varpi^{L+1,0} = C_{\text{tol}}, \quad (7.11)$$

where C_{tol} is a (coupling) tolerance and where K_d is the number of desired iterations.⁸ If the error tolerance is not met in the desired number of iterations, the contraction constant $\eta^{L+1,K}$ is too large. Accordingly, one can solve for a new smaller step size, under the assumption that S is constant,

$$\Delta t_{\text{tol}} = \Delta t \left(\frac{\left(\frac{C_{\text{tol}}}{\varpi^{L+1,0}} \right)^{\frac{1}{p K_d}}}{\left(\frac{\varpi^{L+1,K}}{\varpi^{L+1,0}} \right)^{\frac{1}{p K}}} \right). \quad (7.12)$$

The assumption that S is constant is not critical, since the time steps are to be recursively refined and unrefined

throughout the simulation. Clearly, the expression in Eq. 7.12 can also be used for time step enlargement, if convergence is met in less than K_d iterations.⁹

Appendix 3: Second-Order Temporal Discretization

Following Zohdi [89–103], discretization of temporally second-order equations can be illustrated by considering

$$\ddot{\mathbf{U}} = \dot{\mathbf{V}} = \boldsymbol{\Psi}(\mathbf{U}). \quad (8.1)$$

Expanding the field \mathbf{V} in a Taylor series about $t + \phi \Delta t$ we obtain

$$\begin{aligned} \mathbf{V}(t + \Delta t) &= \mathbf{V}(t + \phi \Delta t) + \frac{d\mathbf{V}}{dt}|_{t+\phi\Delta t} (1 - \phi) \Delta t \\ &\quad + \frac{1}{2} \frac{d^2\mathbf{V}}{dt^2}|_{t+\phi\Delta t} (1 - \phi)^2 (\Delta t)^2 + \mathcal{O}((\Delta t)^3) \end{aligned} \quad (8.2)$$

and

$$\begin{aligned} \mathbf{V}(t) &= \mathbf{V}(t + \phi \Delta t) - \frac{d\mathbf{V}}{dt}|_{t+\phi\Delta t} \phi \Delta t + \frac{1}{2} \frac{d^2\mathbf{V}}{dt^2}|_{t+\phi\Delta t} \phi^2 (\Delta t)^2 \\ &\quad + \mathcal{O}((\Delta t)^3) \end{aligned} \quad (8.3)$$

Subtracting the two expressions yields

$$\frac{d\mathbf{V}}{dt}|_{t+\phi\Delta t} = \frac{\mathbf{V}(t + \Delta t) - \mathbf{V}(t)}{\Delta t} + \hat{\mathcal{O}}(\Delta t), \quad (8.4)$$

where $\hat{\mathcal{O}}(\Delta t) = \mathcal{O}((\Delta t)^2)$, when $\phi = \frac{1}{2}$. Thus, inserting this into the governing equation yields

$$\mathbf{V}(t + \Delta t) = \mathbf{V}(t) + \Delta t \boldsymbol{\Psi}(t + \phi \Delta t) + \hat{\mathcal{O}}((\Delta t)^2). \quad (8.5)$$

Note that adding a weighted sum of Eqs. 8.2 and 8.3 yields

$$\mathbf{V}(t + \phi \Delta t) = \phi \mathbf{V}(t + \Delta t) + (1 - \phi) \mathbf{V}(t) + \mathcal{O}((\Delta t)^2), \quad (8.6)$$

which will be useful shortly. Now expanding the field \mathbf{U} in a Taylor series about $t + \phi \Delta t$ we obtain

$$\begin{aligned} \mathbf{U}(t + \Delta t) &= \mathbf{U}(t + \phi \Delta t) + \frac{d\mathbf{U}}{dt}|_{t+\phi\Delta t} (1 - \phi) \Delta t \\ &\quad + \frac{1}{2} \frac{d^2\mathbf{U}}{dt^2}|_{t+\phi\Delta t} (1 - \phi)^2 (\Delta t)^2 + \mathcal{O}((\Delta t)^3) \end{aligned} \quad (8.7)$$

and

⁷ For the class of problems under consideration, due to the linear dependency on Δt , $p \approx 1$.

⁸ Typically, K_d is chosen to be between five to ten iterations.

⁹ At the implementation level, since the exact solution is unknown, the following relative error term is used, $\varpi^{L+1,K} \stackrel{\text{def}}{=} \|\mathbf{W}^{L+1,K} - \mathbf{W}^{L+1,K-1}\|$.

$$\begin{aligned} \mathbf{U}(t) &= \mathbf{U}(t + \phi\Delta t) - \frac{d\mathbf{U}}{dt}|_{t+\phi\Delta t}\phi\Delta t + \frac{1}{2}\frac{d^2\mathbf{U}}{dt^2}|_{t+\phi\Delta t}\phi^2(\Delta t)^2 \\ &\quad + \mathcal{O}((\Delta t)^3). \end{aligned} \quad (8.8)$$

Subtracting the two expressions yields

$$\frac{\mathbf{U}(t + \Delta t) - \mathbf{U}(t)}{\Delta t} = \mathbf{V}(t + \phi\Delta t) + \hat{\mathcal{O}}(\Delta t). \quad (8.9)$$

Inserting Eq. 8.6 yields

$$\begin{aligned} \mathbf{U}(t + \Delta t) &= \mathbf{U}(t) + (\phi\mathbf{V}(t + \Delta t) + (1 - \phi)\mathbf{V}(t))\Delta t \\ &\quad + \hat{\mathcal{O}}((\Delta t)^2). \end{aligned} \quad (8.10)$$

and thus using Eq. 8.5 yields

$$\begin{aligned} \mathbf{U}(t + \Delta t) &= \mathbf{U}(t) + \mathbf{V}(t)\Delta t + \phi(\Delta t)^2\Psi(\mathbf{U}(t + \phi\Delta t)) \\ &\quad + \hat{\mathcal{O}}((\Delta t)^2). \end{aligned} \quad (8.11)$$

The term $\Psi(\mathbf{U}(t + \phi\Delta t))$ can be handled in two main ways:

- $\Psi(t + \phi\Delta t) \approx \Psi(\phi\mathbf{U}(t + \Delta t) + (1 - \phi)\mathbf{U}(t))$ or
- $\Psi(t + \phi\Delta t) \approx \phi\Psi(\mathbf{U}(t + \Delta t)) + (1 - \phi)\Psi(\mathbf{U}(t))$.

The differences are quite minute between either of the above, thus, for brevity, we choose the latter. In summary, we have the following:

$$\begin{aligned} \mathbf{U}(t + \Delta t) &= \mathbf{U}(t) + \mathbf{V}(t)\Delta t + \phi(\Delta t)^2(\phi\Psi(\mathbf{U}(t + \Delta t)) \\ &\quad + (1 - \phi)\Psi(\mathbf{U}(t))) + \hat{\mathcal{O}}((\Delta t)^2). \end{aligned} \quad (8.12)$$

We note that

- When $\phi = 1$, then this is the (implicit) Backward Euler scheme, which is very stable (very dissipative) and $\mathcal{O}((\Delta t)^2)$ locally in time,
- When $\phi = 0$, then this is the (explicit) Forward Euler scheme, which is conditionally stable and $\mathcal{O}((\Delta t)^2)$ locally in time,
- When $\phi = 0.5$, then this is the (implicit) “Midpoint” scheme, which is stable and $\hat{\mathcal{O}}((\Delta t)^2) = \mathcal{O}((\Delta t)^3)$ locally in time.

In summary, we have for the velocity¹⁰

$$\mathbf{V}(t + \Delta t) = \mathbf{V}(t) + \Delta t(\phi\Psi(\mathbf{U}(t + \Delta t)) + (1 - \phi)\Psi(\mathbf{U}(t))) \quad (8.13)$$

and for the position

$$\begin{aligned} \mathbf{U}(t + \Delta t) &= \mathbf{U}(t) + \mathbf{V}(t + \phi\Delta t)\Delta t \\ &= \mathbf{U}(t) + (\phi\mathbf{V}(t + \Delta t) + (1 - \phi)\mathbf{V}(t))\Delta t, \end{aligned} \quad (8.14)$$

or more explicitly

¹⁰ In order to streamline the notation, we drop the cumbersome $\mathcal{O}(\Delta t)$ -type terms.

$$\begin{aligned} \mathbf{U}(t + \Delta t) &= \mathbf{U}(t) + \mathbf{V}(t)\Delta t + \phi(\Delta t)^2(\phi\Psi(\mathbf{U}(t + \Delta t)) \\ &\quad + (1 - \phi)\Psi(\mathbf{U}(t))). \end{aligned} \quad (8.15)$$

In iterative (recursion) form

$$\begin{aligned} \mathbf{U}^{L+1,K} &= \underbrace{(\phi\Delta t)^2\Psi(\mathbf{U}^{L+1,K-1})}_{\mathcal{G}(\mathbf{U}^{L+1,K-1})} \\ &\quad + \underbrace{\mathbf{U}^L + \mathbf{V}^L\Delta t + (\Delta t)^2\phi(1 - \phi)\Psi(\mathbf{U}^L)}_{\mathcal{R}} \end{aligned} \quad (8.16)$$

Remark Applying this scheme to the balance of linear momentum continuum formulation, under infinitesimal deformations, $\nabla_X \cdot \boldsymbol{\sigma} + \mathbf{f} = \rho \frac{\partial^2 \mathbf{u}}{\partial t^2}$ we use $\Psi(\mathbf{u}(t)) = \frac{\nabla_X \cdot \boldsymbol{\sigma} + \mathbf{f}}{\rho}$, and must apply the (iterative) process introduced earlier to all nodes in the system.

References

1. Ames WF (1977) Numerical methods for partial differential equations, 2nd edn. Academic Press, New York
2. Avci B, Wriggers P (2012) A DEM-FEM coupling approach for the direct numerical simulation of 3D particulate flows. J Appl Mech 79:010901-1–010901-7
3. Bolintineanu DS, Grest GS, Lechman JB, Pierce F, Plimpton SJ, Schunk PR (2014) Particle dynamics modeling methods for colloid suspensions. Comput Part Mech 1(3):321–356
4. Ahmad Z, Rasekh M, Edirisinghe M (2010) Electrohydrodynamic direct writing of biomedical polymers and composites. Macromol Mater Eng 295:315–319
5. Akisanya AR, Cocks ACF, Fleck NA (1997) The yield behavior of metal powders. Int J Mech Sci 39:1315–1324
6. Anand L, Gu C (2000) Granular materials: constitutive equations and shear localization. J Mech Phys Solids 48:1701–1733
7. Axelsson O (1994) Iterative solution methods. Cambridge University Press, Cambridge
8. Bianco M, Bilardi G, Pesavento F, Pucci G, Schrefler BA (2003) A frontal solver tuned for fully coupled non-linear hydro-thermo-mechanical problems. Int J Numer Meth Eng 57(1801): 1818
9. Brown S, Abou-Chedid G (1994) Yield behavior of metal powder assemblages. J Mech Phys Solids 42:383–398
10. Campello EMB, Zohdi TI (2014) A computational framework for simulation of the delivery of substances into cells. Int J Numer Methods Biomed Eng 30(11):1132–1152
11. Campello EMB, Zohdi TI (2014) Design evaluation of a particle bombardment system to deliver substances into cells. Comput Mech Eng Sci 98(2):221–245
12. Cante J, Davalos C, Hernandez JA, Oliver J, Jonsen P, Gustafsson G, Haggblad HA (2014) PFEM-based modeling of industrial granular flows. Comput Part Mech 1(1):47–70
13. Carbonell JM, Onate E, Suarez B (2010) Modeling of ground excavation with the particle finite element method. J Eng Mech ASCE 136:455–463
14. Choi S, Park I, Hao Z, Holman HY, Pisano AP, Zohdi TI (2010) Ultra-fast self-assembly of micro-scale particles by open channel flow. Langmuir 26(7):4661–4667
15. Choi S, Stassi S, Pisano AP, Zohdi TI (2010) Coffee-ring effect-based three dimensional patterning of micro, nanoparticle assembly with a single droplet. Langmuir 26(14):11690–11698

16. Choi S, Jamshidi A, Seok TJ, Zohdi TI, Wu MC, Pisano AP (2012) Fast, high-throughput creation of size-tunable micro, nanoparticle clusters via evaporative self-assembly in picoliter-scale droplets of particle suspension. *Langmuir* 28(6): 3102–3111
17. Choi S, Pisano AP, Zohdi TI (2013) An analysis of evaporative self-assembly of micro particles in printed picoliter suspension. *J Thin Solid Films* 537(30):180–189
18. Deckard C (1986) Method and apparatus for producing parts by selective sintering. U.S. Patent 4,863,538
19. Demko M, Choi S, Zohdi TI, Pisano AP (2012) High resolution patterning of nanoparticles by evaporative self-assembly enabled by in-situ creation and mechanical lift-off of a polymer template. *Appl Phys Lett* 99:253102-1–253102-3
20. Demko MT, Cheng JC, Pisano AP (2010) High-resolution direct patterning of gold nanoparticles by the microfluidic molding process. *Langmuir* 26:16710–16714
21. Domas F (1997) Eigenschaft profile und Anwendungsübersicht von EPE und EPP. Technical report of the BASF Company
22. Donev A, Cisse I, Sachs D, Variano EA, Stillinger F, Connelly R, Torquato S, Chaikin P (2004a) Improving the density of jammed disordered packings using ellipsoids. *Science* 303(5662): 990–993
23. Donev A, Stillinger FH, Chaikin PM, Torquato S (2004b) Unusually dense crystal ellipsoid packings. *Phys Rev Lett* 92:255506
24. Duran J (1997) Sands, powders and grains. In: An introduction to the physics of granular matter. Springer, Berlin
25. Dwivedi G, Wentz T, Sampath S, Nakamura T (2010) Assessing process and coating reliability through monitoring of process and design relevant coating properties. *J Therm Spray Technol* 19:695–712
26. Fleck NA (1995) On the cold compaction of powders. *J Mech Phys Solids* 43:1409–1431
27. Fuller SB, Wilhelm EJ, Jacobson JM (2002) Ink-jet printed nanoparticle microelectromechanical systems. *J Microelectromech Syst* 11:54–60
28. Gamota D, Brazis P, Kalyanasundaram K, Zhang J (2004) Printed organic and molecular electronics. Kluwer Academic Publishers, New York
29. Gethin DT, Lewis RW, Ransing RS (2003) A discrete deformable element approach for the compaction of powder systems. *Model Simul Mater Sci Eng* 11(1):101–114
30. Ghosh S (2011) Micromechanical analysis and multi-scale modeling using the voronoi cell finite element method. CRC Press/Taylor & Francis, Boca Raton
31. Ghosh S, Dimiduk D (2011) Computational methods for microstructure-property relations. Springer NY, Berlin
32. Gu C, Kim M, Anand L (2001) Constitutive equations for metal powders: application to powder forming processes. *Int J Plast* 17:147–209
33. Hashin Z, Shtrikman S (1962) On some variational principles in anisotropic and nonhomogeneous elasticity. *J Mech Phys Solids* 10:335–342
34. Hashin Z (1983) Analysis of composite materials: a survey. *ASME J Appl Mech* 50:481–505
35. Householder R (1979) Molding process. U.S. Patent 4,247,508
36. Huang Y, Leu MC, Mazumdar J, Dommez A (2015) Additive manufacturing: current state, future potential, gaps and needs, and recommendation. *J Manuf Sci Eng* 137:014001–1
37. Huang D, Liao F, Molesa S, Redinger D, Subramanian V (2003) Plastic-compatible low-resistance printable gold nanoparticle conductors for flexible electronics. *J Electrochem Soc* 150(7): G412–417
38. Hull C (1984) Apparatus for production of three-dimensional objects by stereolithography. U.S. Patent 4,575,330
39. Ignaczak J, Ostoja-Starzewski M (2010) Thermoelasticity with finite wave speeds. Oxford mathematical monographs
40. Jikov VV, Kozlov SM, Oleinik OA (1994) Homogenization of differential operators and integral functionals. Springer, Berlin
41. Kachanov LM (1986) Introduction to continuum damage mechanics. Martinus Nijhoff, Dordrecht
42. Kachanov M (1993) Elastic solids with many cracks and related problems. *Adv Appl Mech*, vol 30. Academic Press, New York, p 259
43. Kachanov M, Tsukrov I, Shafiro B (1994) Effective moduli of solids with cavities of various shapes. *Appl Mech Rev* 47:S151–S174
44. Kachanov M, Sevostianov I (2005) On the quantitative characterization of microstructures and effective properties. *Int J Solids Struct* 42:309–336
45. Kansa A, Torquato S, Stillinger F (2002) Diversity of order and densities in jammed hard-particle packings. *Phys Rev E* 66:041109
46. Labra C, Onate E (2009) High-density sphere packing for discrete element method simulations. *Commun Numer Methods Eng* 25(7):837–849
47. Leonardi A, Wittel FK, Mendoza M, Herrmann HJ (2014) Coupled DEM-LBM method for the free-surface simulation of heterogeneous suspensions. *Comput Part Mech* 1(1):3–13
48. Lewis RW, Gethin DT, Yang XSS, Rowe RC (2005) A combined finite-discrete element method for simulating pharmaceutical powder tabletting. *Int J Numer Methods Eng* 62(853):869
49. Lewis RW, Schrefler BA, Simoni L (1992) Coupling versus uncoupling in soil consolidation. *Int J Numer Anal Methods Geomech* 15:533–548
50. Lewis RW, Schrefler BA (1998) The finite element method in the static and dynamic deformation and consolidation of porous media, 2nd edn. Wiley, Hoboken
51. Liu Y, Nakamura T, Dwivedi G, Valarezo A, Sampath S (2008) Anelastic behavior of plasma sprayed zirconia coatings. *J Am Ceram Soc* 91:4036–4043
52. Liu Y, Nakamura T, Srinivasan V, Vaidya A, Gouldstone A, Sampath S (2007) Nonlinear elastic properties of plasma sprayed zirconia coatings and associated relationships to processing conditions. *Acta Mater* 55:4667–4678
53. Martin P (2009) Handbook of deposition technologies for films and coatings, 3rd edn. Elsevier, Amsterdam
54. Martin P (2011) Introduction to surface engineering and functionally engineered materials. Scrivener and Elsevier. *J Vac Sci Technol A2(2)*:500
55. Maxwell JC (1867) On the dynamical theory of gases. *Philos Trans Soc Lond* 157:49
56. Maxwell JC (1873) A treatise on electricity and magnetism, 3rd edn. Clarendon Press, Oxford
57. Mura T (1993) Micromechanics of defects in solids, 2nd edn. Kluwer Academic Publishers, Dordrecht
58. Nakanishi H, Bishop KJM, Kowalczyk B, Nitzan A, Weiss EA, Tretiakov KV, Apodaca MM, Klajn R, Stoddart JF, Grzybowski BA (2009) Photoconductance and inverse photoconductance in thin films of functionalized metal nanoparticles. *Nature* 460: 371–375
59. Nakamura T, Liu Y (2007) Determination of nonlinear properties of thermal sprayed ceramic coatings via inverse analysis. *Int J Solids Struct* 44:1990–2009
60. Nakamura T, Qian G, Berndt CC (2000) Effects of pores on mechanical properties of plasma sprayed ceramic coatings. *J Am Ceram Soc* 83:578–584
61. Nemat-Nasser S, Hori M (1999) Micromechanics: overall properties of heterogeneous solids, 2nd edn. Elsevier, Amsterdam
62. Onate E, Idelsohn SR, Celigueta MA, Rossi R (2008) Advances in the particle finite element method for the analysis of fluid-

- multibody interaction and bed erosion in free surface flows. *Comput Methods Appl Mech Eng* 197(19–20):1777–1800
63. Onate E, Celigueta MA, Idelsohn SR, Salazar F, Surez B (2011) Possibilities of the particle finite element method for fluid-soil-structure interaction problems. *Comput Mech* 48:307–318
 64. Onate E, Celigueta MA, Latorre S, Casas G, Rossi R, Rojek J (2014) Lagrangian analysis of multiscale particulate flows with the particle finite element method. *Comput Part Mech* 1(1):85–102
 65. Pöschel T, Schwager T (2004) Computational granular dynamics. Springer, Berlin
 66. Joseph DD, Preziosi L (1989) Heat waves. *Rev Modern Phys* 61:41–74
 67. Qian G, Nakamura T, Berndt CC (1998) Effects of thermal gradient and residual stresses on thermal barrier coating fracture. *Mech Mater* 27:91–110
 68. Ransing RS, Lewis RW, Gethin DT (2004) Using a deformable discrete-element technique to model the compaction behaviour of mixed ductile and brittle particulate systems. *Philos Trans R Soc Ser A Math Phys Eng Sci* 362(1822):1867–1884
 69. Rayleigh JW (1892) On the influence of obstacles arranged in rectangular order upon properties of a medium. *Philos Mag* 32:481–491
 70. Rojek J, Labra C, Su O, Onate E (2012) Comparative study of different discrete element models and evaluation of equivalent micromechanical parameters. *Int J Solids Struct* 49:1497–1517. doi:[10.1016/j.ijsolstr.2012.02.032](https://doi.org/10.1016/j.ijsolstr.2012.02.032)
 71. Rojek J (2014) Discrete element thermomechanical modelling of rock cutting with valuation of tool wear. *Comput Part Mech* 1(1):71–84
 72. Samarasinghe SR, Pastoriza-Santos I, Edirisinghe MJ, Reece MJ, Liz-Marzan LM (2006) Printing gold nanoparticles with an electrohydrodynamic direct write device. *Gold Bull* 39:48–53
 73. Schrefler BA (1985) A partitioned solution procedure for geothermal reservoir analysis. *Commun Appl Numer Methods* 1:53–56
 74. Sevostianov I, Kachanov M (2000) Modeling of the anisotropic elastic properties of plasma-sprayed coatings in relation to their microstructure. *Acta Mater* 48(6):1361–1370
 75. Sevostianov I, Kachanov M (2001) Thermal conductivity of plasma sprayed coatings in relation to their microstructure. *J Therm Spray Technol* 9(4):478–482
 76. Sevostianov I, Kachanov M (2001) Plasma-sprayed ceramic coatings: anisotropic elastic and conductive properties in relation to the microstructure; cross-property correlations. *Mater Sci Eng A* 297:235–243
 77. Sevostianov I, Gorbatikh L, Kachanov M (2001) Recovery of information of porous/microcracked materials from the effective elastic/conductive properties. *Mater Sci Eng A* 318:1–14
 78. Sevostianov I, Kachanov M (2008) Connections between elastic and conductive properties of heterogeneous materials. *Adv Appl Mech* 42:69–253
 79. Sirringhaus H, Kawase T, Friend RH, Shimoda T, Inbasekaran M, Wu W, Woo EP (2000) High-resolution inkjet printing of all-polymer transistor circuits. *Science* 290:2123–2126
 80. Tatzel H (1996) Grundlagen der Verarbeitungstechnik von EPP-Bewährte und neue Verfahren. Technical report of the BASF Company
 81. Torquato S (2002) Random heterogeneous materials: microstructure & macroscopic properties. Springer, New York
 82. Turska E, Schrefler BA (1994) On consistency, stability and convergence of staggered solution procedures. *Rend Mat acc Lincei Rome S* 9(5):265–271
 83. Wang X, Schrefler BA (1998) A multifrontal parallel algorithm for coupled thermo-hydro-mechanical analysis of deforming porous media. *Int J Numer Methods Eng* 43(1069):1083
 84. Wang JZ, Zheng ZH, Li HW, Huck WTS, Sirringhaus H (2004) Dewetting of conducting polymer inkjet droplets on patterned surfaces. *Nat Mater* 3:171–176
 85. Widom B (1966) Random sequential addition of hard spheres to a volume. *J Chem Phys* 44:3888–3894
 86. Young DM (1950) Iterative methods for solving partial difference equations of elliptic type. Doctoral thesis. Harvard University
 87. Zienkiewicz OC (1984) Coupled problems & their numerical solution. In: Lewis RW, Bettes P, Hinton E (eds) Numerical methods in coupled systems. Wiley, Chichester, pp 35–58
 88. Zienkiewicz OC, Paul DK, Chan AHC (1988) Unconditionally stable staggered solution procedure for soil-pore fluid interaction problems. *Int J Numer Methods Eng* 26:1039–1055
 89. Zohdi TI (2002) An adaptive-recursive staggering strategy for simulating multifield coupled processes in microheterogeneous solids. *Int J Numer Methods Eng* 53:1511–1532
 90. Zohdi TI (2003) Genetic design of solids possessing a random-particulate microstructure. *Philos Trans R Soc Math Phys Eng Sci* 361(1806):1021–1043
 91. Zohdi TI (2004) Modeling and simulation of a class of coupled thermo-chemo-mechanical processes in multiphase solids. *Comput Methods Appl Mech Eng* 193(6–8):679–699
 92. Zohdi TI (2007) Computation of strongly coupled multifield interaction in particle-fluid systems. *Comput Methods Appl Mech Eng* 196:3927–3950
 93. Zohdi TI (2008) On the computation of the coupled thermo-electromagnetic response of continua with particulate microstructure. *Int J Numer Methods Eng* 76:1250–1279
 94. Zohdi TI (2010) Simulation of coupled microscale multiphysical-fields in particulate-doped dielectrics with staggered adaptive FDTD. *Comput Methods Appl Mech Eng* 199:79–101
 95. Zohdi TI (2013) Rapid simulation of laser processing of discrete particulate materials. *Arch Comput Methods Eng* 1–17. doi:[10.1007/s11831-013-9092-6](https://doi.org/10.1007/s11831-013-9092-6)
 96. Zohdi TI (2014) A computational modeling framework for heat transfer processes in laser-induced dermal tissue removal. *Comput Mech Eng* 98(3):261–277
 97. Zohdi TI (2014) Additive particle deposition and selective laser processing—a computational manufacturing framework. *Comput Mech* 54:171–191
 98. Zohdi TI (2015) Rapid computation of statistically-stable particle/feature ratios for consistent substrate stresses in printed flexible electronics. *J Manuf Sci Eng ASME. MANU-14-1476*. doi:[10.1115/1.4029327](https://doi.org/10.1115/1.4029327)
 99. Zohdi TI (2015) On the thermal response of a laser-irradiated powder particle in additive manufacturing. *CIRP J Manuf Sci Technol* 10:77–83
 100. Zohdi TI (2015) Modeling and simulation of cooling-induced residual stresses in heated particulate mixture depositions. *Comput Mech* 56:613–630
 101. Zohdi TI, Wriggers P (2008) Introduction to computational micromechanics. Springer, Berlin Second Reprinting
 102. Zohdi TI (2007) Introduction to the modeling and simulation of particulate flows. SIAM (Society for Industrial and Applied Mathematics), Philadelphia
 103. Zohdi TI (2012) Electromagnetic properties of multiphase dielectrics: a primer on modeling, theory and computation. Springer, Berlin